CM^2 MAGAZINE

第 36 期

南方科技大学海洋磁学中心主编

创刊词

海洋是生命的摇篮，是文明的纽带。地球上最早的生命诞生于海洋，海洋里的生命最终进化成了人类，人类的文化融合又通过海洋得以实现。人因海而兴。

人类对海洋的探索从未停止。从远古时代美丽的神话传说，到麦哲伦的全球航行，再到现代对大洋的科学钻探计划，海洋逐渐从人类敬畏崇拜幻想的精神寄托演变成可以开发利用与科学研究的客观存在。其中，上个世纪与太空探索同步发展的大洋科学钻探计划将人类对海洋的认知推向了崭新的纬度：深海（deep sea）与深时（deep time）。大洋钻探计划让人类知道，奔流不息的大海之下，埋藏的却是亿万年的地球历史。它们记录了地球板块的运动，从而使板块构造学说得到证实；它们记录了地球环境的演变，从而让古海洋学方兴未艾。

在探索海洋的悠久历史中，从大航海时代的导航，到大洋钻探计划中不可或缺的磁性地层学，磁学发挥了不可替代的作用。这不是偶然，因为从微观到宏观，磁性是最基本的物理属性之一，可以说，万物皆有磁性。基于课题组的学科背景和对海洋的理解，我们对海洋的探索以磁学为主要手段，海洋磁学中心因此而生。

海洋磁学中心，简称 CM^2，一为其全名“Centre for Marine Magnetism”的缩写，另者恰与爱因斯坦著名的质能方程 $E = MC^2$ 对称，借以表达我们对科学巨匠的敬仰和对科学的不懈追求。

然而科学从来不是单打独斗的产物。我们以磁学为研究海洋的主攻利器，但绝不仅限于磁学。凡与磁学相关的领域均是我们关注的重点。为了跟踪反映国内外地球科学特别是与磁学有关的地球科学领域的最新研究进展，海洋磁学中心特地主办 CM^2 Magazine，以期与各位地球科学工作者相互交流学习、合作共进！

“海洋孕育了生命，联通了世界，促进了发展”。 21 世纪是海洋科学的时代，由陆向海，让我们携手迈进中国海洋科学的黄金时代

目 录

岩石磁学演绎

第 26 章　磁铁矿和磁赤铁矿

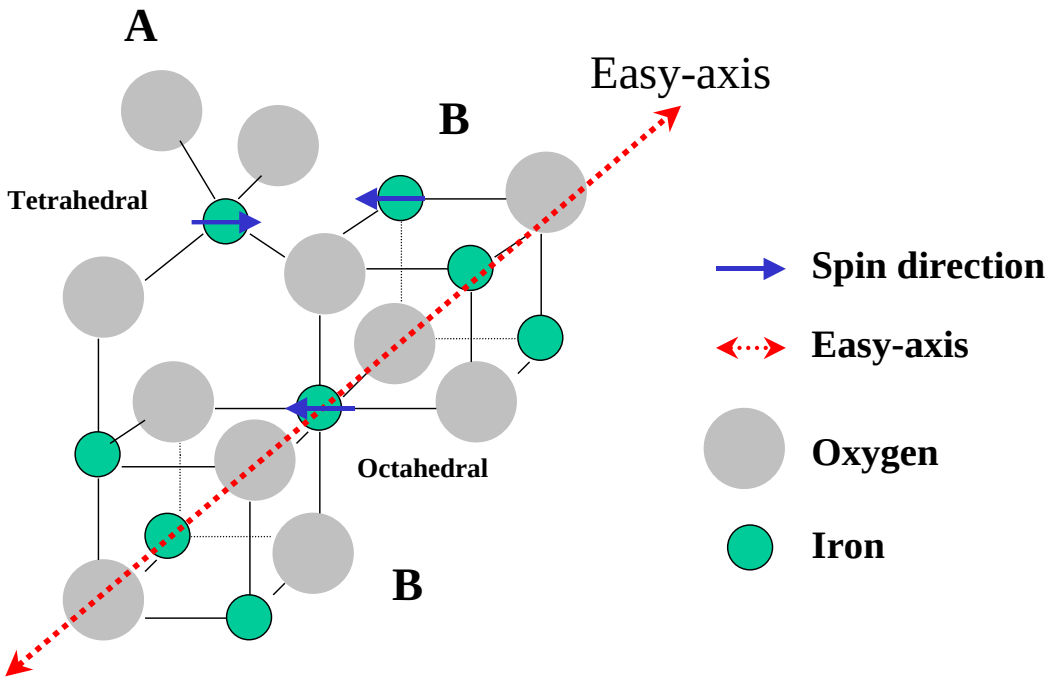

图 1 磁铁矿的晶格结构图

磁铁矿（Fe_3O_4）是磁学研究中的重中之重，它的晶格结构是一种典型的反尖晶石结构。磁铁矿分子中有三个铁离子，其中两个 Fe^{3+}，一个 Fe^{2+}。一个 Fe^{3+} 单独存在于 A 位（A-site），与周边的氧离子形成一个四面体（Tetrahedral）。而在 B 位（B-Site），一个 Fe^{3+}和一个 Fe^{2+}和周边的氧离子一起形成一个八面体（Octahedral）。四面体和八面体中的两个铁离子的磁矩刚好相反，于是互相抵消，独留下八面体中的 Fe^{2+}，这就是磁铁矿的强磁性来源。连接相邻两个八面体对角线方向，就是它的易磁化轴方向。这种由于 A 位和 B 位磁矩不相等，不能相互抵消而形成的磁性叫做亚铁磁性（Ferrimagnetism）。

磁铁矿的内禀性质有：

T_c =578 ℃

M_s = 480 kA/m = 92 Am^2/kg

T_{Verwey} = 120 K （Verwey 转换温度，对应化学计量纯度 100%）

a=8.396 Å （晶格参数）

以上是我们用来鉴别样品中是否存在磁铁矿最有效的参数。

关于居里温度，目前我们有两个方法来确定。

第一种就是磁化率温度曲线（χ-T）。χ-T 曲线测量简单，但是，该曲线还受到粒径分布的影响。大部分情况下，为了避免加热过程中样品被空气中的氧气氧化，加热时通氩气。但是这会造成样品的还原环境，形成很多的细粒磁铁矿。这就使得升温曲线中的出现的磁铁矿的居里点存在多解性。只有在 χ-T 曲线的升温和降温曲线相对可逆的情况下，得出的特殊磁化率峰才代表解阻行为，否则如果降温曲线高于升温曲线，就说明新生成的矿物影响较大。很多初学者会迷惑，为什么在升温过程中看不到矿物转化，而降温曲线却大幅度增加？这是由于新生成的矿物的化学反应发生在 580 ℃之上，此时磁性大幅度降低。但是，在降温过程中，低于居里温度时，它们的磁性就会立刻显示出来。

第二种就是饱和磁化强度温度曲线（J-T）曲线，可以通过居里秤获得。它的好处在于饱和磁化强度和粒径不相关，解释起来相对简单。同时，一般情况下在实验过程中不会加氩气，所以很难加热生成磁铁矿。即便有磁性矿物生成，在加热过程中很快就氧化成赤铁矿。

Verwey 转换是磁铁矿特有的低温性质，对于纯磁铁矿（化学计量纯度）来说，这个温度发生 120 K。如果磁铁矿晶格中掺杂了一点杂质（比如，空位或者 Ti^{4+}），在摩尔浓度小于 4%时，T_V 会随着化学计量纯度的降低而降低。

物理学家对磁铁矿的 Verwey 转化进行了详细的研究。在 120 K 之上，磁铁矿晶格中 A-Site 和 B-Site 之间铁离子中的电子有自由交换行为，从而整体晶格表现为立方体。随着温度的降低，在 120 K 之下，电子变得懒惰，没有多余能量在两个 Sites 之间进行交换，那么晶格结构就变得不对称，从而形成一种单斜结构。

磁铁矿这种晶格结构上的变化，会引起其易磁化轴的变化。也就是说在 120 K 之上的一些易磁化轴，在 120 K 之下就变成难磁化轴，其直接结果就是，磁矩会从难磁化轴发生偏转，寻找临近的易磁化轴。在剩磁上，就表现为磁性变得混乱，被退磁了。反过来也一样，在 120 K 之下获得的剩磁，在通过 T_V 时，由于易磁化轴的变化，磁矩也会部分发生混乱，造成退磁。

实验结果表明，磁铁矿的低温剩磁在 T_V 确实会大幅度变化，其变化幅度与其磁畴状态相关。对于 MD 颗粒，可下降 90%以上。随着粒径变小，SD 颗粒的剩磁下降幅度最小。对于 SP 颗粒是什么情形？SP 颗粒会逐渐解阻其剩磁，在 120 K 并不会产生特殊行为。正是由于这种和磁畴的关系，磁铁矿的 Low-T SIRM 热退磁曲线还可以被用来分离 MD、SD、SP 颗粒的剩磁。比如，在 T_V 大幅度下降的剩磁为 MD 主导，逐渐解阻的剩磁是 SP 的行为，在 300 K 剩下的剩磁则是 SD 颗粒主导。

磁铁矿的 T_V 并不是一个常量，随着其晶格结构中杂质的增多，T_V 会逐渐下降。当含有杂质时，磁铁矿可以表示为 $Fe_{3-3\delta}O_4$（对应氧化程度时的晶格空位 Vacancy）或者 $Fe_{3-x}Ti_xO_4$（对应着钛磁铁矿）。实际上，只要有一点杂质，比如 4 mol%的 Ti^{4+}，T_V 就下降到 80 K。而且，T_V 的变化还遵循两个独立的趋势，在 110-110 K 之间，不存在 T_V 行为。所以，测量自然介质，我们观察不到 115 K 的 T_V，因为它根本就不存在。

有一种细菌叫做磁细菌，它们的体内会生成一串串的纳米级磁铁矿，被称之为磁小体。经过测量其 T_V，发现 T_V 一般为 110 K。即使对新鲜的样品也是这个结果。这说明，磁小体磁铁矿的化学计量纯度不是 100%。高倍 TEM 观测发现，磁小体磁铁矿晶格中确实存在着 Vacancy。

压力对 T_V 也产生很大的影响，如果磁铁矿受到压力作用，T_V 也会向低值移动。比如，我们如果研究陨石坑里的磁铁矿，会经常发现存在两种磁铁矿，一类磁铁矿的 T_V 为 120 K，一类的磁铁矿 T_V 为 110 K。如果不是磁小体的影响，那么后者就对应着压力影响。我们可以把样品加热一下，后者晶格内存在的应力会释放，这个 110 K 的 T_V 也会随之消失。磁小体的低值 T_V 可不会被加热处理改变。

磁铁矿被氧化时，其晶格里的 Fe^{2+} 会被氧化成 Fe^{3+}，同时晶格内产生缺陷（Vacancy）。当 Fe^{2+} 全部被氧化成 Fe^{3+} 时，其分子式就会和赤铁矿完全一致 Fe_2O_3，但是其晶格结构还和磁铁矿相同，这种矿物叫做磁赤铁矿。

磁赤铁矿的主要特征：

M_s = 380 kA/m

a = 8.337 Å

对于小颗粒磁赤铁矿，具有热不稳定性，在 300 ℃之上会慢慢转化为赤铁矿。与黑色的磁铁矿相比，其颜色偏红。不具有 Verwey 转换。

CM2 研究进展

70ka 以来黑海古地磁记录的 Nowegian-Greenland Sea、Laschmaps 和 Mono Lake 地磁漂移事件

过去几十年中，海洋沉积物记录的古地磁结果不断扩展我们对地磁场长期变化的理解，从偶极子场控制下的地磁场长期稳定变化，到地磁漂移和极性倒转事件。本文基于 16 根黑海沉积物钻孔，获得了过去 68.9-14.5 ka 之间具有强度和方向的古地磁记录。年代模型基于放射性碳测年，以及高分辨率的化学元素比值和冰筏碎屑与格林兰冰芯氧同位素记录的‘Dansgaard-Oeschger’ (DO)旋回对比。

黑海古地磁结果记录了 Norwegian-Greenland Sea、Laschamps 和 Mono Lake 地磁漂移事件。这些漂移事件分别位于 64.5 ka, 41.0 ka 和 34.5 ka，具有明显的方向漂移以及相对古强度下降。此外，黑海古地磁结果没有发现 20-17ka 之间可能存在的'Hilina Pali‘漂移事件。为了进一步讨论地磁场变化特征，黑海古地磁结果被转换成一个分量平行于轴向偶极子场（GAD-parallel），两个分量与 GAD 方向正交，仅表示非轴向偶极子场（non-GAD）贡献。因此，Laschamps 和 Norwegian-Greenland Sea 漂移事件出现极低的 GAD-parallel 分量，而 Mono Lake 却存在较大的 non-GAD 分量贡献。尤其值得注意的是，GAD-parallel 组分在 Laschamps 事件时期出现负值，指示完全的地磁场倒转。

进而，基于黑海和全球其他五个区域古地磁数据，我们建立了基于球谐函数的地磁场模型 GGFSS07.1。结合高分辨率的黑海古地磁结果和 GGFSS70.1 模型，我们发现 Norwegian-Greenland Sea(~64.5 ka)事件期间，尽管缺少显著的方向漂移记录，但是轴向偶极子场快速衰减并伴随着较弱的非偶极子场特征。Laschamp 事件具有完全的地磁场方向倒转，并且在地磁北极漂移至南极区域时，出现了短暂的轴向偶极子场增强。Mono Lake 事件主要由非偶极子场控制，地磁场方向出现明显漂移，但是轴向偶极子场并未显著下降。Hilina Pali(~18 ka)事件时期，轴向偶极子场具有一定的衰减，但是在黑海古地磁记录并未发现地磁场漂移特征。

综上，黑海古地磁结果反映地磁场特征受控于偶极子场和非偶极子场具有高度变化的叠加。黑海古地磁中的 GAD-parallel 和 non-GAD 分量变化，以及地磁场模型，均指示地磁场漂移事件受控于偶极子场的衰减，尽管非偶极子场可能没有显著变化。

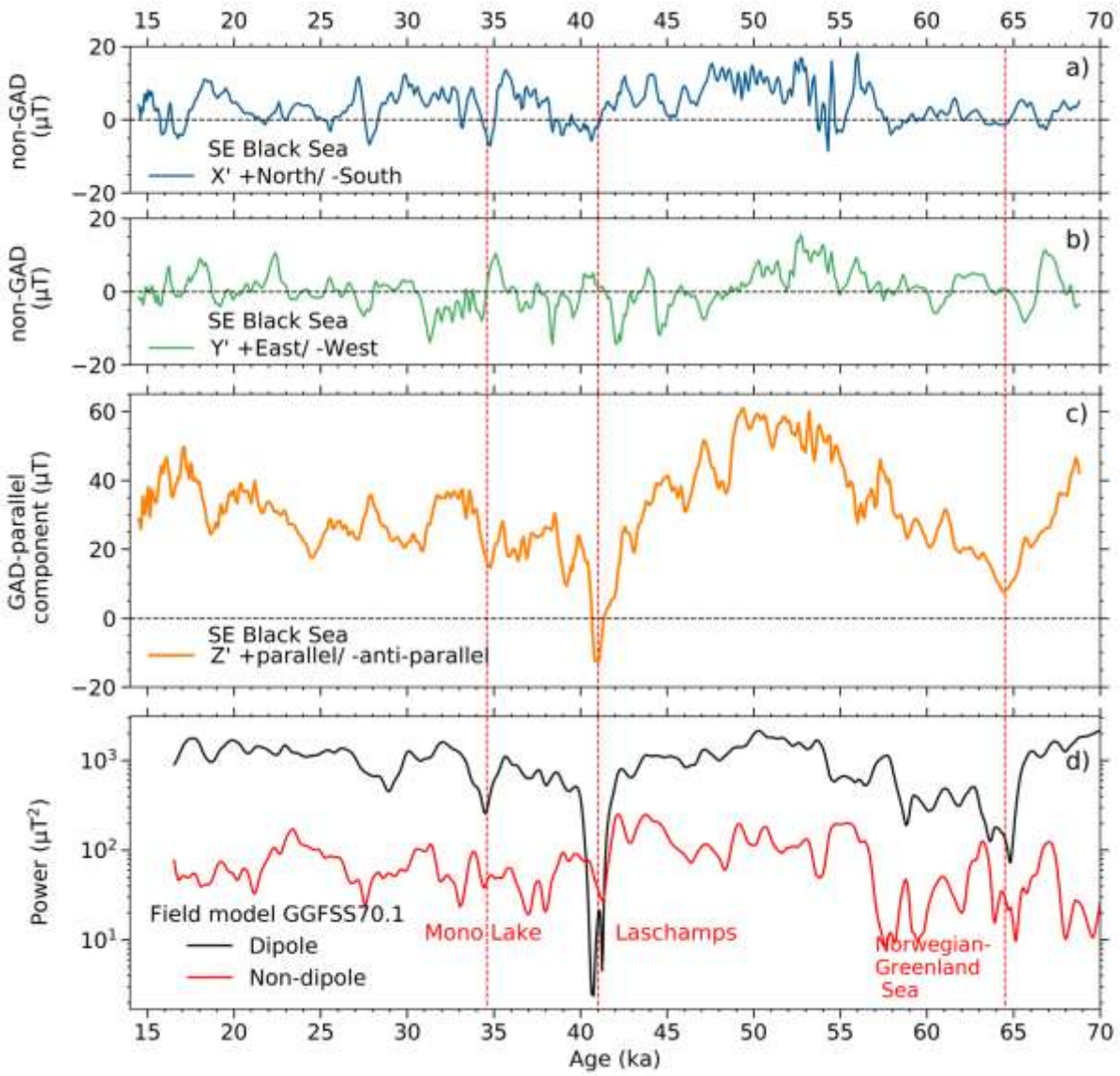

图 1. 黑海古地磁结果被换成 a)沿着 NS (X')方向分量，b)沿着 EW (Y')方向分量和 c)与轴向偶极子场(GAD)方向平行分量。d)GGFSS70.1 地磁场模型反映的偶极子场和非偶极子场在地表的变化。

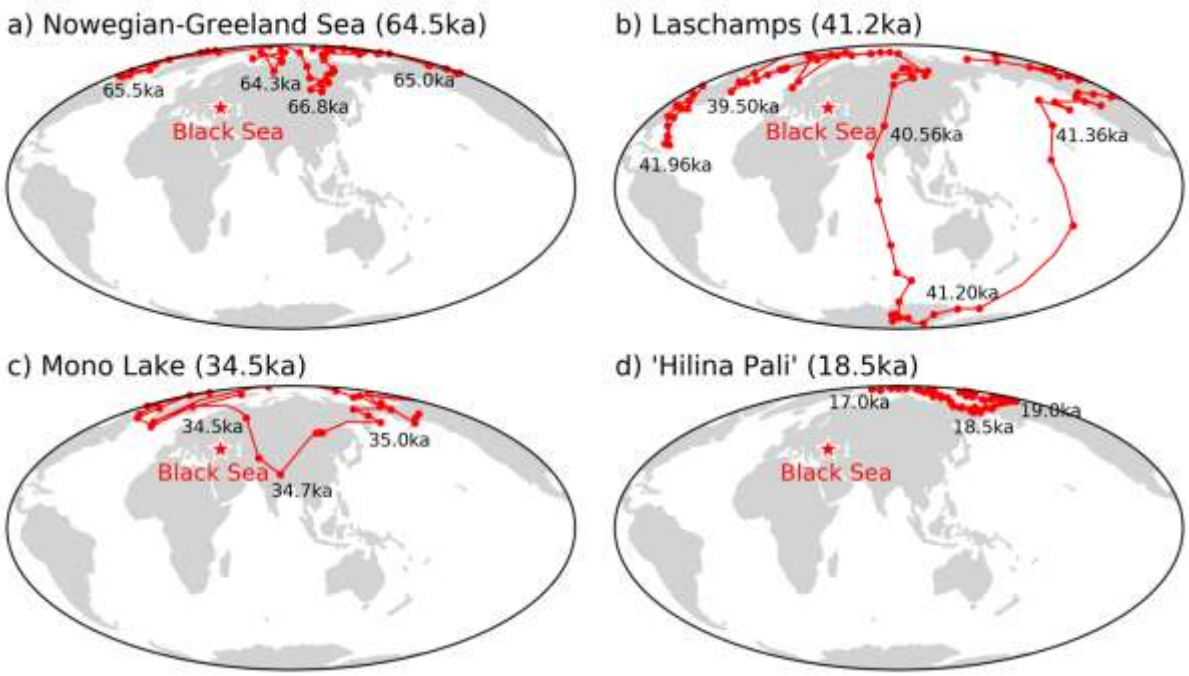

图 2. 黑海古地磁数据计算的虚拟地磁极(VGP)。a) 69-64 ka 之间的 Norwegian-Greenland Sea 漂移事件。b) 43-39 ka 之间的 Laschamps 漂移事件。c) 36-33 ka 之间的 Mono Lake 漂移事件。d) 20-17 ka 之间可能的'Hilina Pali 漂移事件'。

参考文献

Liu, J., Nowaczyk, N.R., Panovska, S., Korte, M., Arz, H.W., 2020. The Norwegian‐Greenland Sea, the Laschamps and the Mono Lake excursions recorded in a Black Sea sedimentary sequence spanning from 68.9 to 14.5 ka. J. Geophys. Res. Solid Earth. https://doi.org/10.1029/2019JB019225

文献导读

1. 绿色撒哈拉沙漠的结束放大了亚洲东南部中晚全新世大干旱

翻译人：仲义 zhongy@sustech.edu.cn

Michael L.Griffiths, Kathleen R. Johnson, Francesco S. R. Pausata et al., **End of Green Sahara amplified mid- to late Holocene megadroughts in mainland Southeast Asia** [J]. Nature Communication, 2020, 11, 4204.

https://doi.org/10.1038/s41467-020-17927-6

摘要：在 5 到 4 千年前，严重的干旱化导致了非洲和亚洲部分地区的古代文明的毁坏，然而这些在东南亚大陆的极端气候的程度还没被仔细研究。尽管考古学的证据表明，这一时期，该地区的人类居住模式发生了变化。作者报道了来自石笋古气候的证据表明，在东南亚地区全新世中后期季风降雨大幅减少，这与绿色撒哈拉沙漠末期终止和非洲季风减弱一致。通过一组模拟实验表明，在绿色撒哈拉沙漠终止时期，植被的减少和沙尘负载的增加使得沃克环流向东移动，并且印度洋降温，并最终导致东南亚大陆季风降水的减弱。我们的研究表明撒哈拉沙漠干旱化引起的植被-风尘气候反馈机制可能会通过海洋-大气遥相关作用直接对于东南亚大陆的社会形态转型产生重要影响。

ABSTRACT: Between 5 and 4 thousand years ago, crippling megadroughts led to the disruption of ancient civilizations across parts of Africa and Asia, yet the extent of these climate extremes in mainland Southeast Asia (MSEA) has never been defined. This is despite archeological evidence showing a shift in human settlement patterns across the region during this period. We report evidence from stalagmite climate records indicating a major decrease of monsoon rainfall in MSEA during the mid- to late Holocene, coincident with African monsoon failure during the end of the Green Sahara. Through a set of modeling experiments, we show that reduced vegetation and increased dust loads during the Green Sahara termination shifted the Walker circulation eastward and cooled the Indian Ocean, causing a reduction in monsoon rainfall in MSEA. Our results indicate that vegetation-dust climate feedbacks from Sahara drying may have been the catalyst for

societal shifts in MSEA via ocean-atmospheric teleconnections.

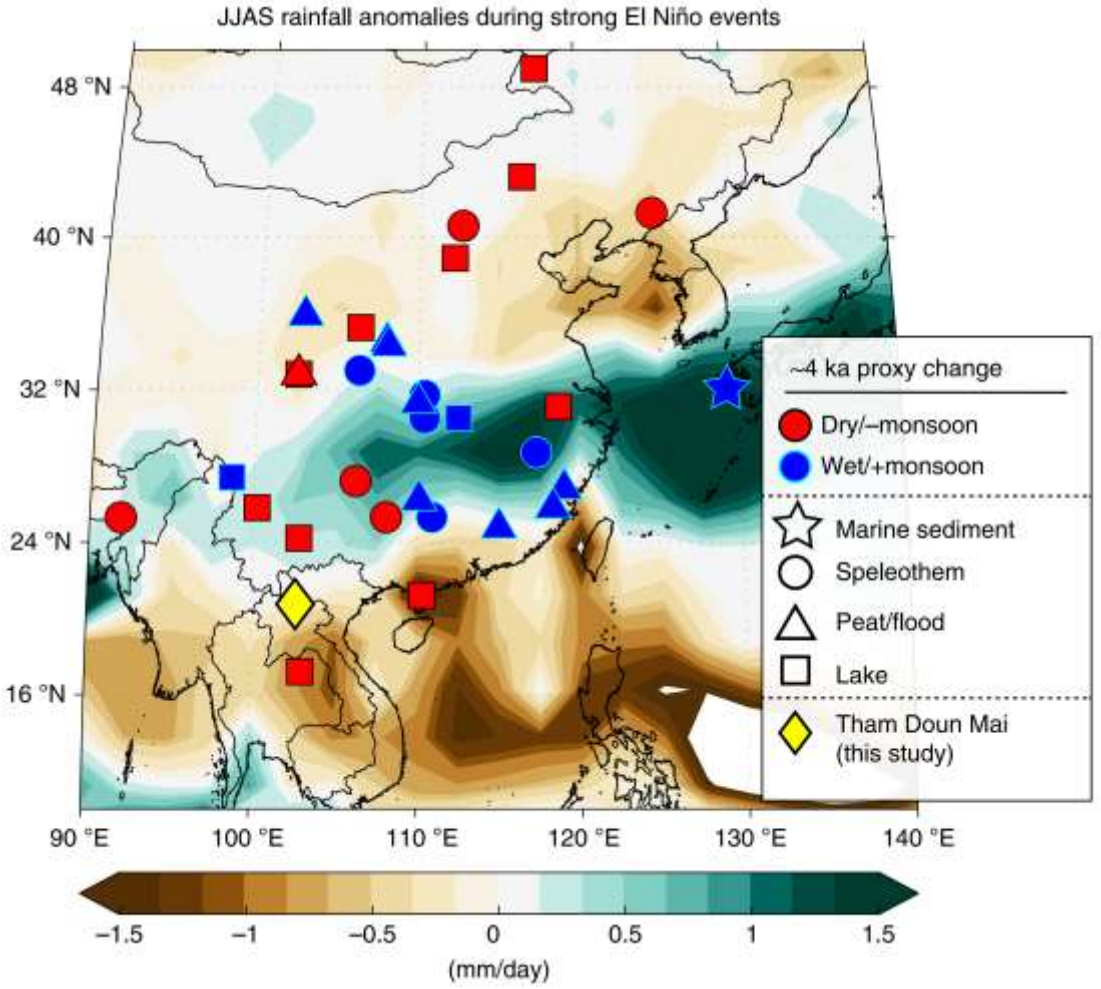

Figure 1. Location of Tham Doun Mai cave (diamond) and other climate proxy sites mentioned in the text. Locations of climate proxy records across East Asia showing relative hydroclimate changes at ≈4 ka as inferred from the synthesis in Supplementary Table 1. Background shading shows Global Precipitation Climatology Project (GPCP) average June-September (JJAS) rainfall anomalies during the large 1982/1983, 1998/1999, and 2015/2016 El Niño events.

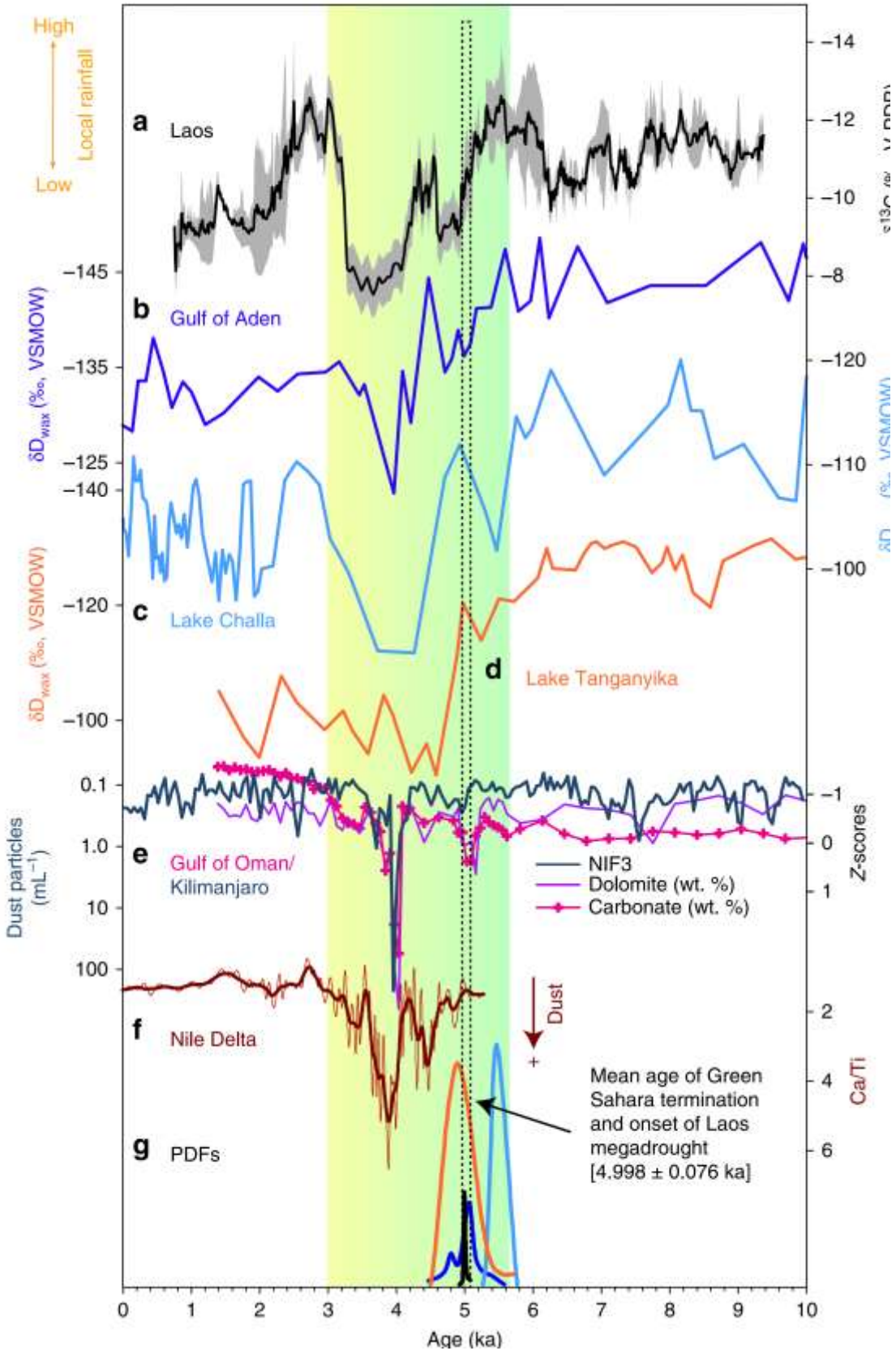

Figure 2. Mainland southeast Asian hydroclimate and end of the Green Sahara. a Northern Laos composite δ13C record (black line) and 1σ uncertainty (gray shading) from Tham Doun Mai

speleothems. b–d δDwax records from marine core P178–15P (Gulf of Aden)3, Lake Challa40, and Lake Tanganyika41.e Percent dolomite (light purple line) and carbonate (pink line) (expressed as standardized Z-scores) from the Gulf of Oman33. Also shown is the dust record (aquamarine line) from Mt. Kilimanjaro ice core KNIF338. f Ca/Ti record of dust deposition in the Nile Delta42. g Color-coded (cyan: Lake Challa; orange: Lake Tanganyika; black: Tham Doun Mai; blue: Gulf of Aden) probability density function (PDF) output from the Bayesian change-point algorithm39. Vertical color bar indicates the transition from a wet to a dry Sahara between 5.5 and 3.5 ka2,3.

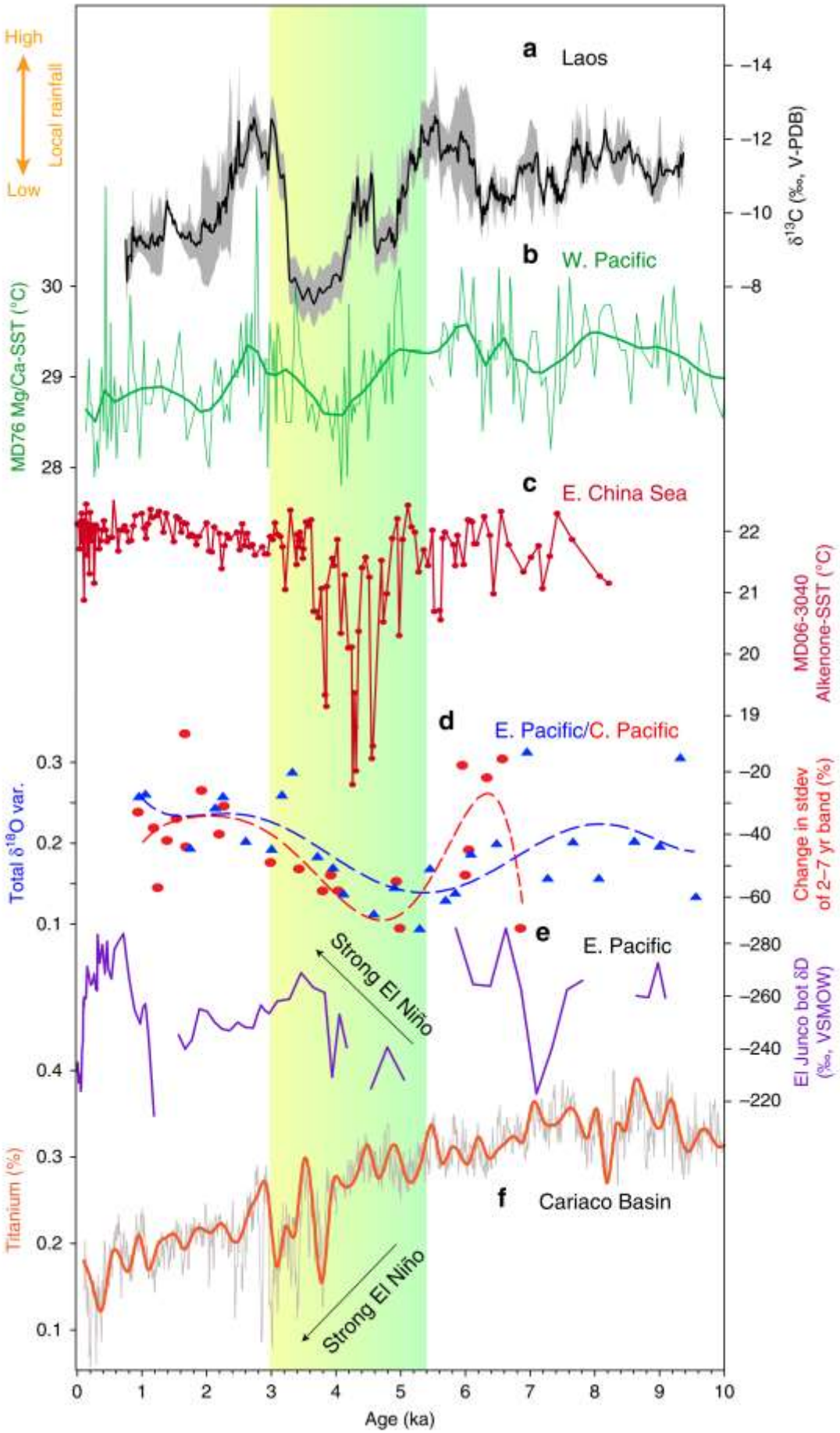
High
Local rainfall
Low
a Laos
b W. Pacific
c E. China Sea
d E. Pacific/C. Pacific
e E. Pacific
f Cariaco Basin
Strong El Niño
Strong El Niño
δ13C (‰, V-PDB)
MD76 Mg/Ca-SST (°C)
MD06-3040 Alkenone-SST (°C)
Total δ18O var.
Change in stdev of 2–7 yr band (%)
El Junco bot δD (‰, VSMOW)
Titanium (%)
Age (ka)

Figure 3. Mainland southeast Asian hydroclimate and ENSO variability. a Northern Laos composite $\delta^{13}C$ record (black line) and 1σ uncertainty (gray shading) from Tham Doun Mai speleothems. b, c Mg/Ca- and alkenone-inferred sea-surface temperature (SST) records from western Pacific marine cores MD7643 and MD06–304073, respectively. d $\delta^{18}O$ variance (var.) of individual G. ruber planktonic foraminifera from core V21–30 (blue triangles; eastern Pacific)74 and relative ENSO variance changes inferred from fossil coral $\delta^{18}O$ [calculated from sliding 30-yr windows of the standard deviation (stdev) of the 2- to 7-year band, and plotted as percent (%) differences from 1968–1998 C.E. intervals of modern coral $\delta^{18}O$] in Fanning Island and Christmas Island (red circles) located in the central Pacific55. Dashed lines show 6th order polynomial regression. e El Junco (Galapagos) δD of botryococcenes56 (bot), interpreted to reflect shifts in ENSO variance. f Bulk titanium content of marine sediments from ODP site 100275 where lower values indicate drier conditions typical of El Niño events. Vertical color bar indicates the transition from a wet to a dry Sahara between 5.5 and 3.5 ka2,3.

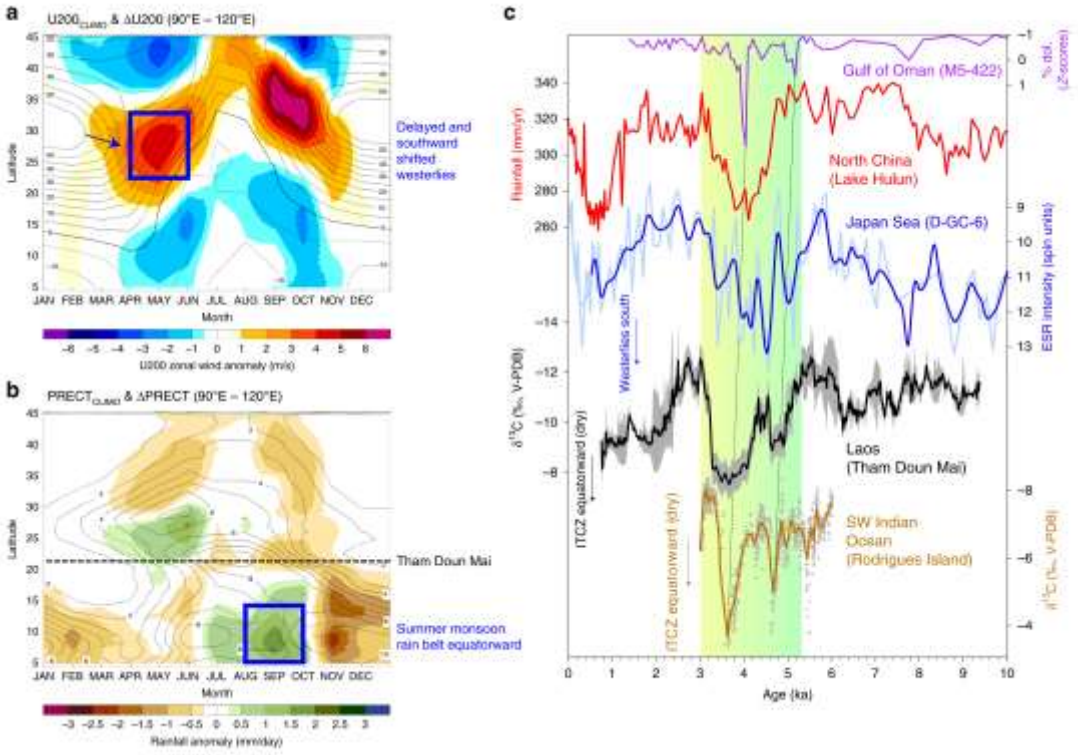

Figure 4. Seasonal shifts in the westerlies and precipitation across East Asia between dry and wet Sahara. a, b Hovmöller diagrams of climatological U200 winds and precipitation for wet Sahara and its anomalies (contours: MHGS+RD climatology; shading: difference between MHPMIP and MHGS+RD

experiments). c Support for the model simulations is provided by the paleoclimate archives, which show drier conditions in North China (red) due to a southward shift in the westerlies (blue; inferred from ESR intensity of silt-sized quartz grains in sediments from the Japan Sea) and equatorward contraction of the ITCZ during boreal summer (black; this study) and austral summer (brown). Vertical color bar indicates the transition from a wet to a dry Sahara between 5.5 and 3.5 ka.

2. 评估彗星碰撞和火山喷发对古新世-始新世极热期气候扰动的贡献

翻译人：蒋晓东 jiangxd@sustech.edu.cn

Liu Z Y, Horton D E, Tabor C., Assessing the Contributions of Comet Impact and Volcanism Toward the Climate Perturbations of the Paleocene‐Eocene Thermal Maximum [J]. Geophysical Research letters, 2020, 46, 798–806

https://doi.org/10.1029/2019GL084818

摘要：古新世–始新世极热事件（PETM）期间具有显著的全球碳同位素负漂移特征，反应了数以万亿吨的较轻的碳释放到大气中去。然而轻碳同位素的来源仍然存在争议。本研究对两处古新世–始新世边界使用多种地球化学指标进行分析，包括锇同位素、汞、硫和铂族元素。数据表明彗星碰撞和火山活动很可能对古新世–始新世期间环境扰动具有贡献。此外，地球系统模型的模拟结果表明平流层中相当于碰撞的量级的硫酸盐气溶胶很可能引起了短暂的变冷和沉积减少。

ABSTRACT: The Paleocene-Eocene Thermal Maximum is marked by a prominent negative carbon‐isotope excursion, reflecting the injection of thousands of gigatons of isotopically light carbon into the atmosphere. The sources of the isotopically light carbon remain poorly constrained. Utilizing a multiproxy geochemical analysis (osmium isotopes, mercury, sulfur, and platinum group elements) of two Paleocene-Eocene boundary records, we present evidence that a comet impact and major volcanic activity likely contributed to the environmental perturbations during the Paleocene-Eocene interval. Additionally, Earth system model simulations indicate that stratospheric sulfate aerosols, commensurate with the impact magnitude, were likely to have caused transient cooling and reduced precipitation.

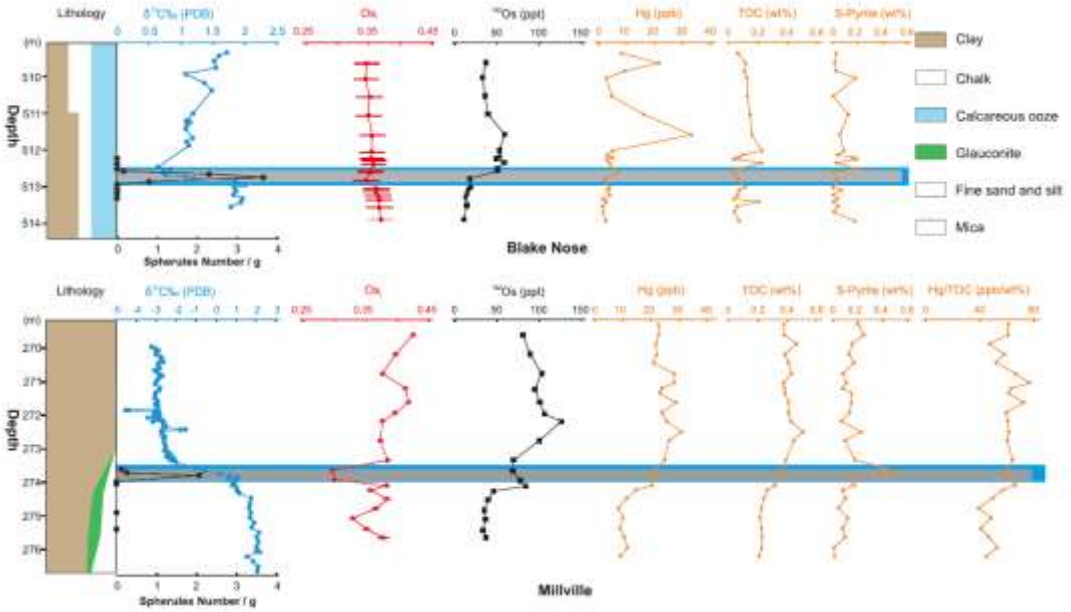

Figure 1. Summary of carbon - isotope, O_{si}, ^{192}Os, Hg, TOC, pyrite sulfur, and Hg/TOC data. Carbon isotope data for Blake Nose are from Katz et al. (1999). Carbon - isotope data for Millville site is from Wright and Schaller (2013). Spherule data are from Schaller et al. (2016). Blue zone marks the base of the negative carbon isotope excursion at the P - E boundary; gray zone marks the interval where spherules are present.

3. 晚奥陶世的生物大灭绝是由火山作用、气候变暖和缺氧引起的，而不是气候变冷和冰川作用导致的

翻译人：冯婉仪 fengwy@sustech.edu.cn

Bond T P G, Grasby S E. Late Ordovician mass extinction caused by volcanism, warming, and anoxia, not cooling and glaciation[J]. Geology, 2020, 48: 777-781. https://doi.org/10.1130/G47377.1

摘要：奥陶纪见证了海洋生物的多样性突然被晚奥陶世生物大灭绝（LOME）所终止。大约85%的物种在两个相隔一百万年的脉冲中灭绝。第一个生物灭绝脉冲发生在赫南特期早期，它与气候变冷和冈瓦纳冰川作用有关。第二个生物灭绝脉冲发生在赫南特期晚期，它由气候变暖和缺氧引起。先前报道的美国内华达、中国南部和波兰的汞峰指示了生物灭绝事件与一个未知的大火成岩省（LIP）有关，但是，汞富集的时间使得与 LIP 有关的生物灭绝的原因存在不同解释，即火山作用导致了气候变冷、变暖或两者兼有。我们报道了 Hg、Mo 和 U 异常、生产力指标的富集因子下降以及在奥陶系-志留系边界层（Dob's Linn, 苏格兰）的两个 LOME 脉冲之间的密切对应关系。这些关系支持了一种生物灭绝的假设，即火山产生的温室气体导致了在卡迪阶-赫南特阶边界的气候变暖，这使得先前存在的深水氧气含量最低带的扩张、生产力的下降以及第一次 LOME 脉冲。在赫南特期，火山的再次喷发导致气候进一步变暖和缺氧，从而出现第二次 LOME 脉冲。与“五次大灭绝”中存在一次罕见的因气候变冷而导致生物灭绝不同，LOME 和其他几次大灭绝类似，都是由火山活动、气候变暖和缺氧引起的。

ABSTRACT: The Ordovician saw major diversification in marine life abruptly terminated by the Late Ordovician mass extinction (LOME). Around 85% of species were eliminated in two pulses 1 m.y. apart. The first pulse, in the basal Hirnantian, has been linked to cooling and Gondwanan glaciation. The second pulse, later in the Hirnantian, is attributed to warming and anoxia. Previously reported mercury (Hg) spikes in Nevada (USA), South China, and Poland implicate an unknown large igneous province (LIP) in the crisis, but the timing of Hg loading has led to different interpretations of the LIP-extinction scenario in which volcanism causes cooling, warming, or both. We report close correspondence between Hg, Mo, and U anomalies, declines in enrichment factors of productivity

proxies, and the two LOME pulses at the Ordovician-Silurian boundary stratotype (Dob's Linn, Scotland). These support an extinction scenario in which volcanogenic greenhouse gases caused warming around the Katian-Hirnantian boundary that led to expansion of a preexisting deepwater oxygen minimum zone, productivity collapse, and the first LOME pulse. Renewed volcanism in the Hirnantian stimulated further warming and anoxia and the second LOME pulse. Rather than being the odd-one-out of the "Big Five" extinctions with origins in cooling, the LOME is similar to the others in being caused by volcanism, warming, and anoxia.

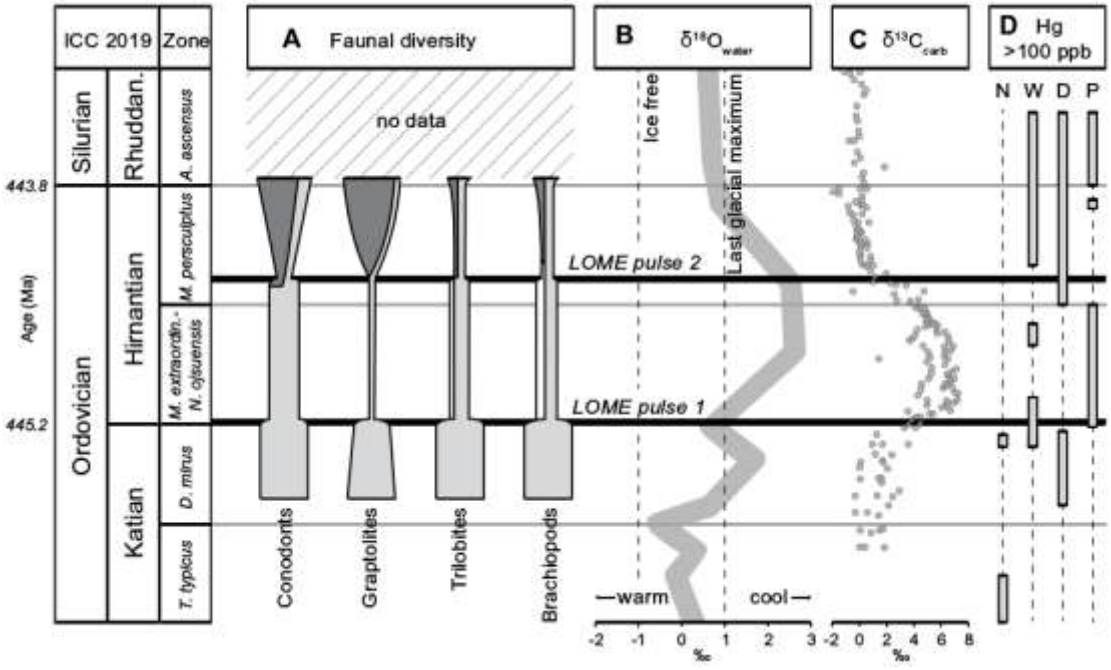

Figure 1. Global features of Late Ordovician mass extinction (LOME). (A) Faunal diversity (Brenchley et al., 2001) including pre-extinction biota (light gray), appearances post–LOME pulse 1 (white), and appearances post–LOME pulse 2 (dark gray). Width gives qualitative sense of within-group diversity changes. (B) $\delta^{18}O$ curve (Finnegan et al., 2011). First LOME pulse occurs at end of phase of warming. (C) Carbonate $\delta^{13}C$ ($\delta^{13}C_{carb}$) records from Laurentia (Kump et al., 1999; LaPorte et al., 2009), which indicate disturbance in carbon cycle associated both LOME pulses. (D) Range of Hg anomalies >100 ppb from Nevada (USA) (N), South China (W — Wangjiawan; D — Dingjiapo), and Poland (P) (Gong et al., 2017; Jones et al., 2017; Smolarek-Lach et al., 2019). Ages (in Ma) from International Chronostratigraphic Chart version 2019/05 (ICC 2019). Rhuddan. — Rhuddanian. Zone refers to graptolite zones (genus abbreviations: T. = Tangyagraptus; D. = Dicellograptus; M. = Metabolograptus;

N. = Normalograptus; A. = Akidograptus).

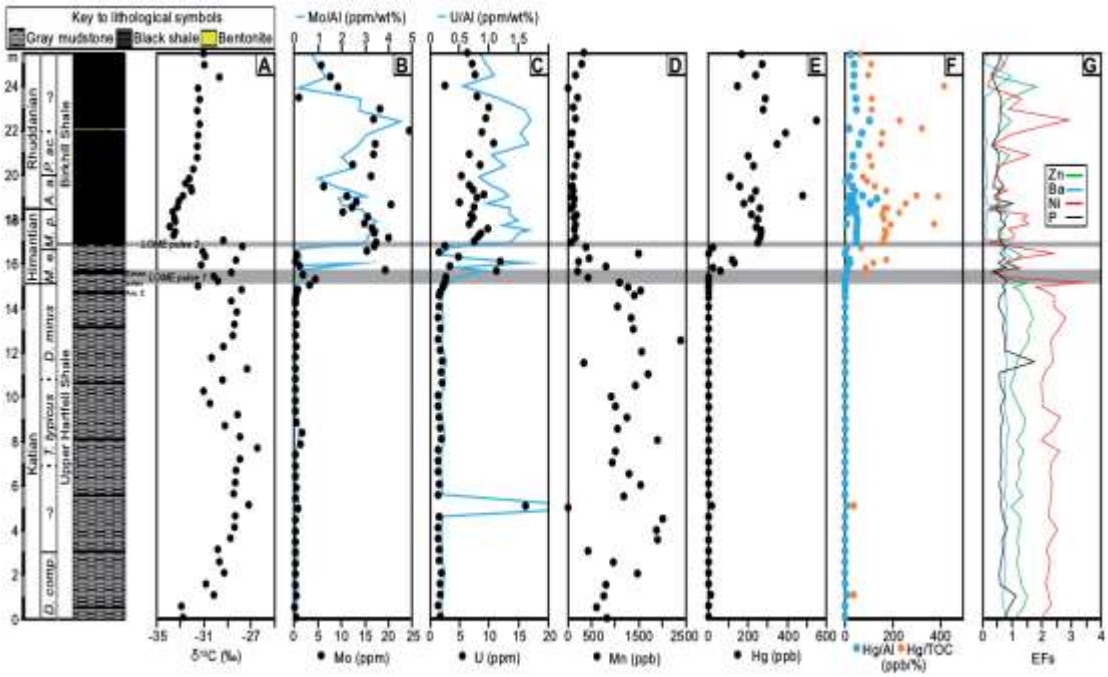

Figure 2. Geochemical data from Dob's Linn (Scotland, UK). (A) Organic $\delta^{13}C$ ($\delta^{13}C_{org}$). (B) Mo and Mo/Al. (C) U and U/Al. (D) Mn. (E) Hg. (F) Hg normalized to total organic carbon (TOC) and total Al. (G) Enrichment factors (EFs) of Zn, Ba, Ni, and P. "ashes" marks level at which numerous thin ash beds appear. Graptolite zonation based on Williams (1988), Rong et al. (2008), and Zhou et al. (2015): D. comp. — Dicellograptus complexus; T. typicus — Tangyagraptus typicus; D. mirus — Dicellograptus mirus; M. e. — Metabolograptus extraordinarius–Normalograptus ojsuensis; M. p. — Metabolograptus persculptus; A. a. — Akidograptus ascensus; P. ac. — Parakidograptus acuminatus. Graptolite bands: Anc. E — Anceps Band E; Extraor. — Extraordinarius Band.

4. 以色列 Golan Heights 火山高原上新世-更新世古地磁和古长期变化的记录

翻译人:李园洁 liyj3@sustech.edu.cn

Behar N, Shaar R, Tauxe L, et al. ***Paleomagnetism and paleosecular variations from the Plio‐Pleistocene Golan Heights volcanic plateau, Israel[J]. Geochemistry, Geophysics, Geosystems****, 2019, 20(9): 4319-4335. https://doi.org/10.1029/ 2019GC008479*

摘要：地磁场长期变化 (PSV) 和时间平均场的统计分析主要基于全球汇总的来自熔岩的古地磁数据。平均倾角异常 (ΔI) 在两个半球表现出不同的趋势，南半球中纬度具有小的正异常 (< 2°) 而北半球中纬度具有大的负异常 (> −5°)。为查明 20° N- 40° N 之间大的ΔI，我们在以色列东北部32-33° N的一个上新世-更新世火山高原Golan-Heights (GH) 获得新的古地磁数据集。GH 数据集包括 91 个熔岩点：40 个 1990 年代获得的和本文的 51 个。熔岩的年代学由 57 个 40Ar/39Ar 年龄约束：39 个前人结果和本文的 18 个。我们发现 1990 年代的数据集可能受到块体旋转的影响，没有完全用于研究 PSV。应用 Fisher 精确度参数和每点的样品个数作为挑选标准计算出上新世-更新世的地磁极与轴向偶极子场一致，倾角异常 (ΔI = −0.4°) 比全球汇总和 PSV 模型预测的更小。用不同的计算方法和挑选标准重新检查全球汇总的倾角异常得出倾角异常值受三个因素影响：(1) 包含有低质量的数据；(2) 纬度分区平均数据；(3) 倾角异常的计算方法。

ABSTRACT：Statistical analysis of geomagnetic paleosecular variation (PSV) and time‐averaged field has been largely based on global compilations of paleomagnetic data from lava flows. These show different trends in the averaged inclination anomaly (ΔI) between the two hemispheres, with small positive (< 2°) anomalies in midsouthern latitudes and large negative (> −5°) anomalies in midnorthern latitudes. To inspect the large ΔI between 20° N and 40° N we augment the global data with a new paleomagnetic data set from the Golan-Heights (GH), a Plio-Pleistocene volcanic plateau in northeast Israel, located at 32-33° N. The GH data set consists of 91 lava flows sites: 40 sites obtained in the 1990s and 51 obtained in this study. The chronology of the flows is constrained by 57 $^{40}Ar/^{39}Ar$ ages: 39 from previous studies and 18 from

this study, which together cover most of the GH plateau. We show that the 1990s data set might be affected by block rotations and does not fully sample PSV. The Plio-Pleistocene pole (86.3° N, 120.8° E, N = 44, k = 25, α_{95} = 4.4°), calculated after applying selection criteria with Fisher precision parameter (k) ⩾ 100 and number of specimens per site (n) ⩾ 5 is consistent with a geocentric axial dipole field and shows smaller inclination anomaly (ΔI = −0.4°) than predicted by global compilations and PSV models. Reexamination of the inclination anomaly in the global compilation using different calculation methods and selection criteria suggests that inclination anomaly values are affected by (1) inclusion of poor quality data, (2) averaging data by latitude bins, and (3) the way the inclination anomaly is calculated.

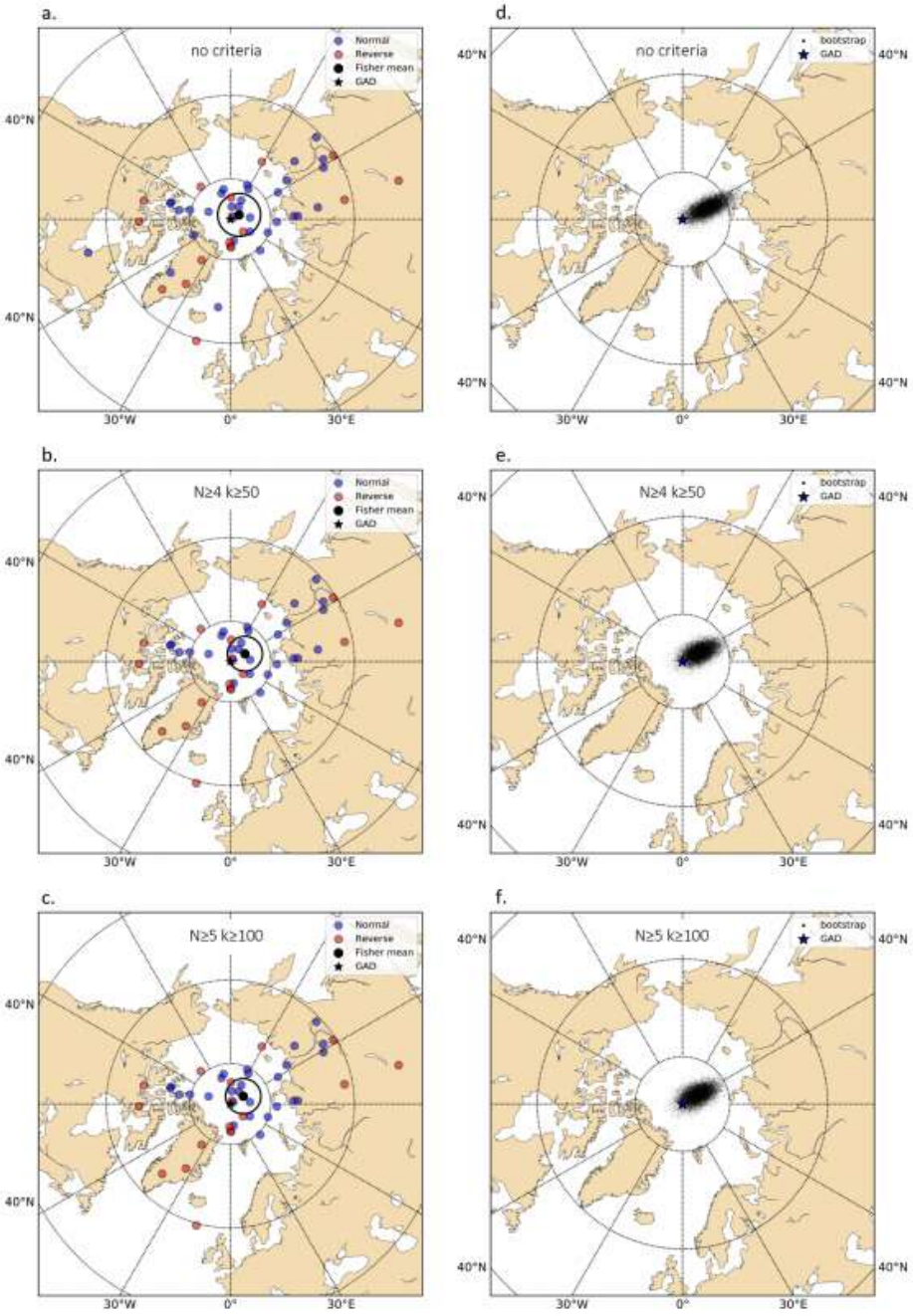

Figure 1. Virtual geomagnetic poles (VGP) and paleomagnetic poles. (a – c) VGPs and paleomagnetic pole calculated using Fisher statistics. (a) No selection criteria are applied; (b) selection criteria are n $\geqslant$ 4, k $\geqslant$ 50; (c) selection criteria are n $\geqslant$ 5, k $\geqslant$ 100. (d – f) Projection of 10,000 bootstrapped Fisher means of pseudo - samples drawn from the data in (a) – (c), respectively. GAD = geocentric axial dipole.

5. 太平洋下地幔中高电导率引起的地磁场微弱变化

翻译人：柳加波

Dumberry M, More C. ***Weak magnetic field changes over the Pacific due to high conductance in lowermost mantle[J]****. Nature Geoscience, 2020, 13(7): 516-520.*

https://doi.org/10.1038/s41561-020-0589-y

摘要：在过去的几个世纪中，太平洋地区地球磁场随时间的变化异常微弱。这与太平洋下方核幔边界附近的液态外核中大规模的流体活动有关。在太平洋地区，这种大规模的流体活动较弱，具有偏心的行星尺度回旋特征，并且广泛避开了该区域。但是，调节这种流动形态的因素尚不清楚。本文，我们展示了地核动力学数值模型的结果，该模型包括与地幔底部不均匀导电层的电磁耦合。结果表明，当该导电层在太平洋下的电导率高于其他地方时，较大的电磁拖曳力会削弱该区地核流体运动，并使行星回旋的流动偏离太平洋。下地幔电导的性质尚不清楚，但是在核幔边界的地形起伏中截留的分层岩心流体是一个可能的解释。

ABSTRACT: For the past few centuries, the temporal variation in Earth's magnetic field in the Pacific region has been anomalously low. The reason for this is tied to large-scale flows in the liquid outer core near the core–mantle boundary, which are weaker under the Pacific and feature a planetary-scale gyre that is eccentric and broadly avoids this region. However, what regulates this type of flow morphology is unknown. Here we present results from a numerical model of the dynamics in Earth's core that includes electromagnetic coupling with a non-uniform conducting layer at the base of the mantle. We show that when the conductance of this layer is higher under the Pacific than elsewhere, the larger electromagnetic drag force weakens the local core flows and deflects the flow of the planetary gyre away from the Pacific. The nature of the lowermost mantle conductance remains unclear, but stratified core fluid trapped within topographic undulations of the core–mantle boundary is a possible explanation.

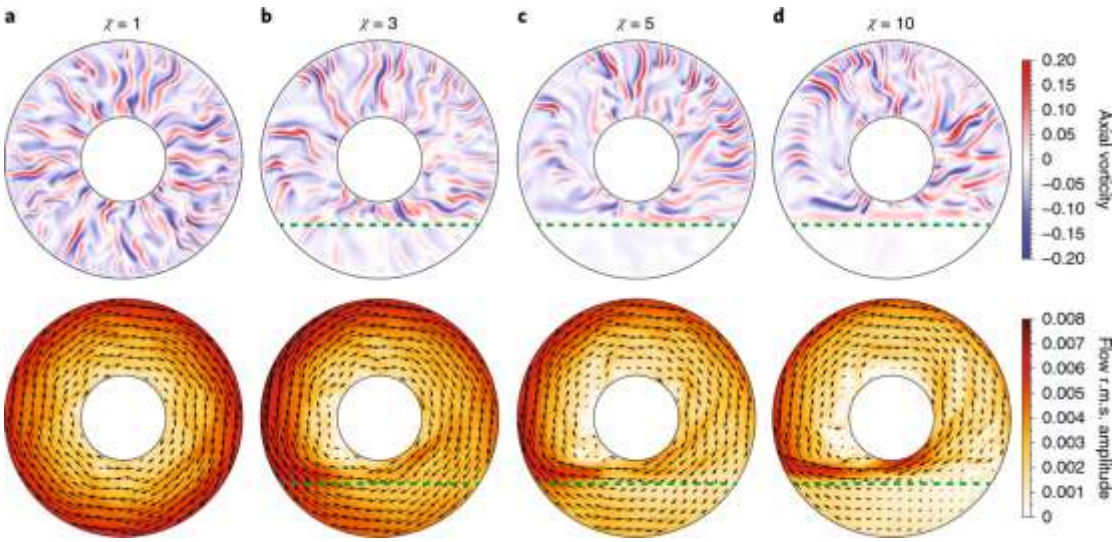

Figure 1. **a**–**d**, Snapshots of the axial vorticity (top row) and time-averaged flow maps (bottom row; colour scale indicates flow speed, arrows show direction) from our quasi-geostrophic model for Ra = 5 × 10^8, Pm = 0.1 and χ = 1 (**a**), 3 (**b**), 5 (**c**) and 10 (**d**). All plots are equatorial planforms. The Pacific region is shown in the bottom section of each planformand is delimited by a dashed green line in **b**, **c** and **d**. The colour scales on the right are common to all four panels and are in non-dimensional units.

6. 南海北缘碎屑沉积物地球化学和 Nd 同位素特征---对构造和物源的指示

翻译人：刘伟 inewway@163.com

Yan Yi，Xia Bin, et al., ***Geochemical and Nd isotope composition of detrital sediments on the north margin of the South China Sea: provenance and tectonic implications****[J].* ***Sedimentology****, 2010, 54(1):1-17. https://doi.org/10.1111/j.1365-3091.2006.00816.x*

摘要：随着喜马拉雅山脉和青藏高原变形影响范围的扩大，西藏东部和西南地区发生了一次重大的区域性水系重组。然而这些变化对区域沉积路径系统的影响还没有得到很好的约束。本文通过对南海北缘莺-琼盆地和南雄盆地沉积岩的地球化学和 Nd 同位素特征的研究，来识别沉积物源区的显著变化。南雄盆地上白垩统至下始新统沉积岩的 Th/Sc、La/Sc、Th/Cr、Th/Co 比值高于 PAAS(后太古界澳大利亚页岩)，Eu/Eu*比值则相对较低。这表明华南地块的古生代沉积岩是主要沉积源区。相比之下，渐新世莺-琼盆地更新世沉积岩表现出微量元素比值在 16.3Ma 和 10.4Ma 之间的突然改变，指示了中中新世物源的转换。莺-琼盆地的 ε Nd 值（-11.1 至-2.1）在 13.8Ma 之前的平均值为-5.6（范围为 2.1 到-7.4），13.8Ma 之后的平均值是-9.3（范围为-8.7 到-11.1）这再次指示了中中新世物源的转换。渐新世期间，裂陷中心向南转移，南海北缘盆地迅速沉降。快速抬升和侵蚀使中生代和新生代的花岗岩为莺-琼盆地提供了大量的花岗质碎屑。接着在 13Ma 发生了物源变化，即局部物源(中新生代构造和岩浆作用形成的断块)的减少，而更古老的大陆物质的物源（主要来自印支到南海西部）贡献增加。

ABSTRACT: A major re-organization of regional drainages in eastern Tibet and southwestern China took place in the Cenozoic as deformation from the growing Himalayas and Tibetan Plateau affected an increasingly wider area. The effects of these changes on the regional sediment routing systems is not well constrained. This study examines the geochemical and Nd signatures of sedimentary rocks from the Ying-Qiong and Nanxiong basins on the northern margin of the South China Sea to constrain and identify any significant changes in sediment source. Upper Cretaceous to Lower Eocene sedimentary rocks in the Nanxiong Basin show higher Th/Sc, La/Sc, Th/Cr and

Th/Co ratios and lower Eu/Eu* ratios than PAAS (post-Archaean Australian Shale), which indicates that Palaeozoic sedimentary rocks of the South China Block were the main basin sediment source. In contrast, Oligocene to Pleistocene sedimentary rocks of the Ying-Qiong Basin show an abrupt change in these trace-element ratios between 16.3 and 10.4 Ma, indicating a mid-Miocene shift in provenance. ε Nd values from the Ying-Qiong Basin (range -11.1 to -2.1) reinforce this, with pre-13.8 Ma sedimentary rocks having average ε Nd of -5.6 (range -2.1 to -7.4), and post-13.8 Ma sedimentary rocks having average ε Nd of -9.3 (range -8.7 to -11.1). During the Oligocene, the centre of rifting transferred south and basins on the north margin of the South China Sea experienced rapid subsidence. Further uplift and erosion then exposed Mesozoic and Cenozoic granites that supplied large amounts of granitic detritus, especially to the Ying-Qiong Basin. Then a change occurred at ca 13 Ma resulting in less input from local sources (i.e. the fault blocks formed by Mesozoic-Cenozoic tectonics and magmatism) to an increasing contribution of older continental material, mostly from Indochina to the west of the South China Sea.

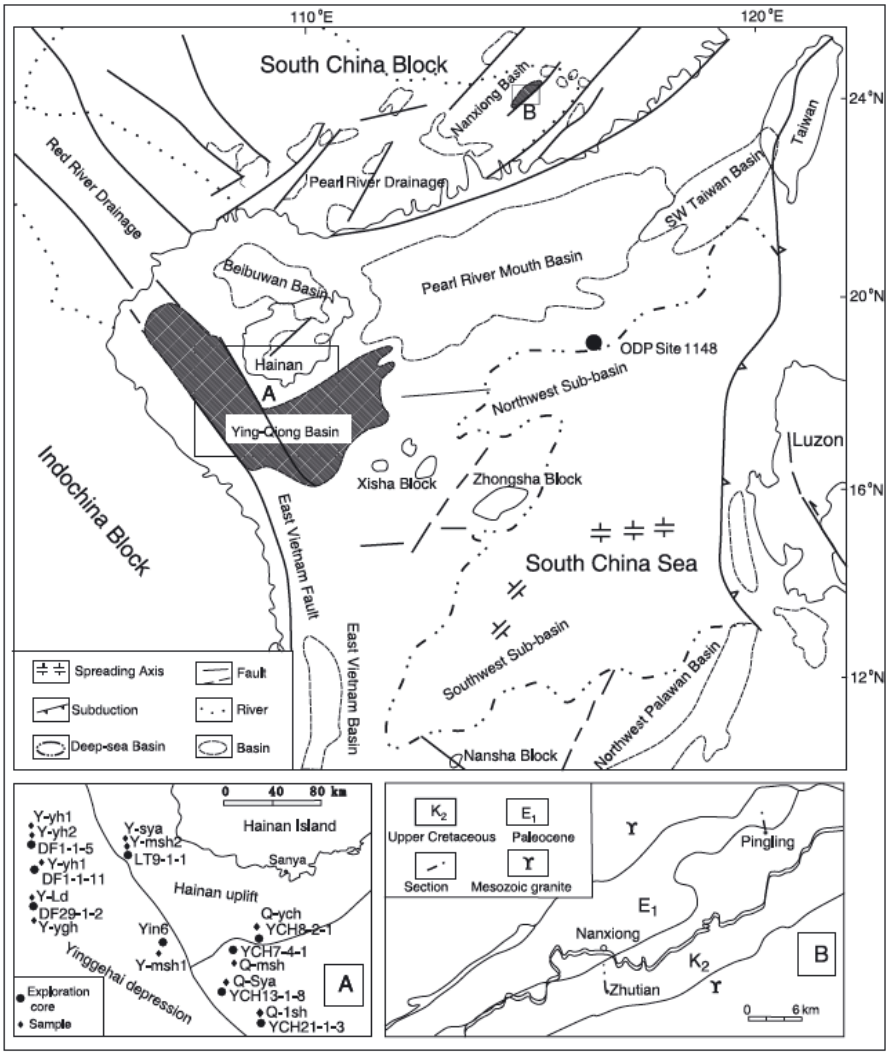

Figure 1. Tectonic setting of the north margin of the South China Sea (modified after Zhou et al., 1995); (A) Location of samples from the Ying-Qiong Basin; (B) location of samples from the Nanxiong Basin.

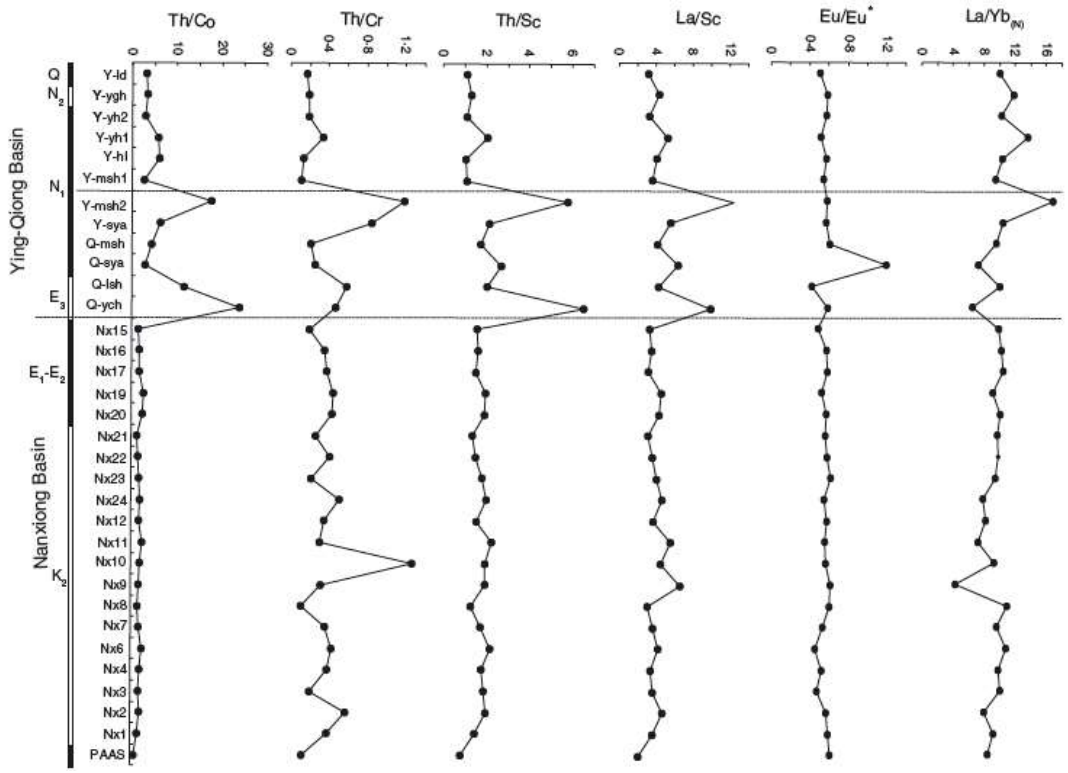

Figure 2. Stratigraphic variation in LaN/YbN, Eu/Eu*, Th/Sc, La/Sc, Th/Cr and Th/Co ratios from the Ying-Qiong and the Nanxiong basins (post-Archaean Australian Shale composition from Taylor & McLennan, 1985).

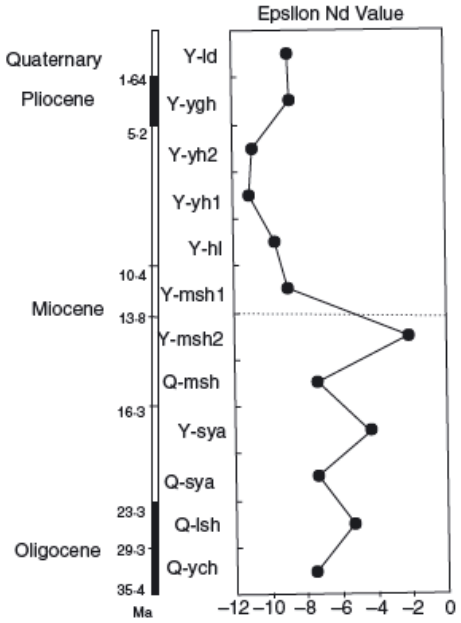

Figure 3. Stratigraphic variation in ε Nd values from the Ying-Qiong Basin.

7. 青藏高原北部及其邻区风成矿床磁学性质的空间和垂直变化:对气候边界划分的启示

翻译人：曹伟 11930854@QQ.com

Zan J, Fang X, Kang J, et al. Spatial and altitudinal variations in the magnetic properties of eolian deposits in the northern Tibetan Plateau and its adjacent regions: Implications for delineating the climatic boundary[J]. Earth-Science Reviews, 2020: 103271

https://doi.org/10.1016/j.earscirev.2020.103271

摘要：划定青藏高原北部及其邻区的气候边界（例如降水与气温）对于了解全球大气环流的动态和中亚地区粉尘过程具有非常重要的意义。然而到目前为止，这一广阔区域的气象资料非常稀少，限制了我们对欧亚大陆区域气候模式和过去气候变化的了解。在本研究中，我们综合了来自上新世晚期、末次冰期旋回和现代风成沉积物的岩石磁学数据，以确定青藏高原北部及其邻区的气候边界。结果表明，不同环境条件下的风成沉积在磁性矿物类型和粒度分布方面有明显的差异。随着气候由湿润向干旱过渡，表层土壤中的磁性矿物逐渐从土壤成因向碎屑成因转变。东祁连山、西帕米尔高原和北天山表层土壤磁性特征的空间和海拔变化揭示出明显的成土强度边界。通过对现有气象资料的分析，推断出的成土强度变化是青藏高原北部半湿润半干旱区与邻区之间的重要气候边界。青藏高原北部主山迎风侧海拔较高的表层土具有较强的成土作用，支持了降水而非温度主导表层土壤磁性增强的结论。此外，对几个晚更新世和末次冰期-间冰期黄土-红粘土序列的对比研究表明，青藏高原东北部及邻区气候梯度的现代空间格局至少自上新世晚期或早更新世以来一致保持。研究结果表明，在暖湿间冰期，青藏高原北部及其邻区的降水梯度变陡。未来，对风成沉积物或表层土壤进行详细的岩石磁学研究可以为青藏高原北部大气环流动力学和古气候模拟提供新的自然边界条件。

ABSTRACT: Delineating the climatic boundary (i.e., of precipitation and temperature) in the northern Tibetan Plateau and along its margins is important for understanding the dynamics of global atmospheric circulation and the processes of dust production in central Asia. To date, however, meteorological data are scarce for this vast region, which limits our understanding of regional climatic patterns and past climatic changes in Eurasia. In the present study, we use a synthesis of both new and published rock magnetic data from the late Pliocene, the last glacialinter

glacial cycle, and modern eolian sediments to identify the climatic boundary in the northern Tibetan Plateau and its adjacent areas. The results demonstrate that eolian deposits under different environmental scenarios exhibit a clear contrast in the type and grain-size distribution of magnetic minerals. With the transition from humid to arid climatic regimes, a gradual shift from magnetic minerals of predominantly pedogenic origin to predominantly detrital origin can be observed in the surface soils. The spatial and altitudinal variations in the magnetic properties of surface soils reveal a distinct boundary of pedogenic intensity in the eastern Qilian Mountains, the western Pamir Plateau and the northern Tianshan Mountains. The inferred variations in pedogenic intensity, combined with analysis of the available meteorological data, demonstrate that the pedogenic boundary represents a critical climatic boundary between sub-humid to semi-arid and arid regions in the northern Tibetan Plateau and the adjacent regions. Stronger pedogenesis occurs in surface soils at higher altitudes on the windward side of the major mountains of the northern Tibetan Plateau, supporting the conclusion that precipitation rather than temperature exerts the dominant effect on the magnetic enhancement of surface soils. In addition, a comparison of several late Pliocene-Pleistocene and last glacial-interglacial loess-red clay sequences suggests that the modern spatial pattern of the climatic gradients in the northeastern Tibetan Plateau and the adjacent regions has been maintained since at least the late Pliocene or early Pleistocene. Moreover, the results demonstrate that during the warm and humid interglacial periods, a steepened rainfall gradient occurred in the northern Tibetan Plateau and its adjacent regions. In the future, detailed rock magnetic investigations of eolian deposits or surface soils could provide new insights into the dynamics of atmospheric circulation and the natural boundary conditions for paleoclimate modeling in the northern Tibetan Plateau.

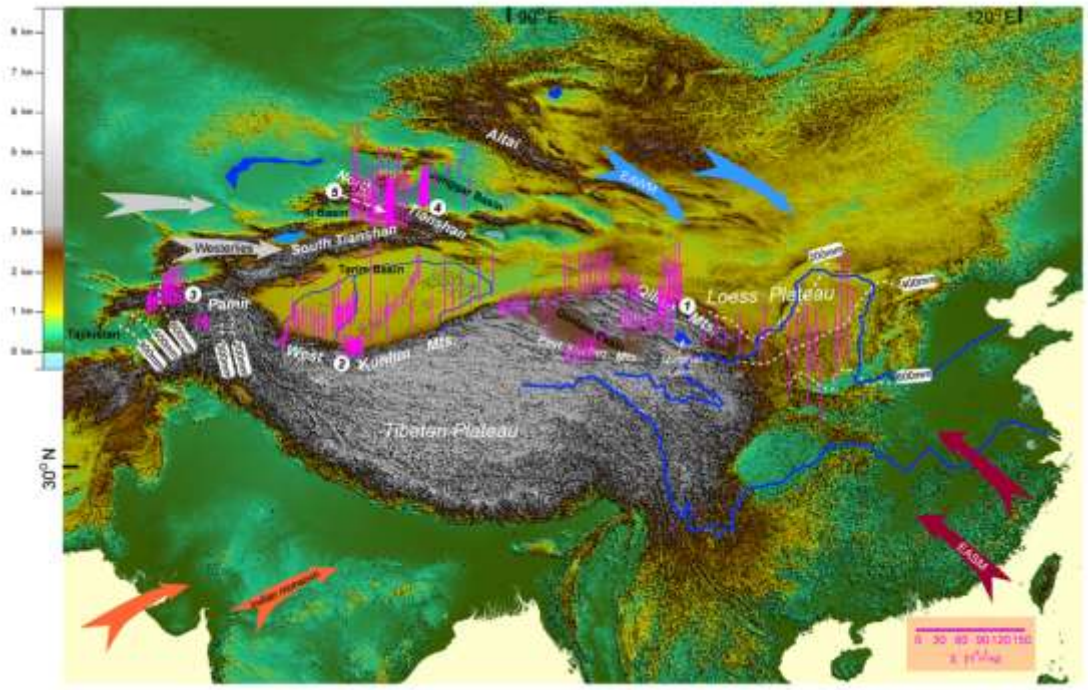

Figure 1. Spatial variation of the magnetic susceptibility (χ) of surface loess and sand samples from the northern Tibetan Plateau and the adjacent regions. The lengths of the magenta lines are proportional to the χ values of the surface samples. The χ values for surface samples from the western Pamir, Ili Basin,Qaidam Basin, Tarim Basin and the Chinese Loess Plateau are previously published data (Jia et al., 2013; Liu et al., 2013; Nie et al., 2014; Zan et al., 2011, 2014, 2015a, 2015b; Zeng et al., 2018; Kang et al., 2020). Note that the surface loess samples from the northern margin of the Qaidam Basin and the southern margin of the Junggar Basin also exhibit relatively high χ values, although the climate in these regions is extremely dry. Circled numbers indicate locations of five altitudinal profiles that were selected for further investigation of the magnetic variations of surface soils under different climatic zones. The white dashed lines are isolines of the modern mean annual precipitation across the western Pamir Plateau and the Chinese Loess Plateau. Digital elevation model map data were obtained from http://www.cgiar-csi.org/data. (For interpretation of the references to colour in this figure legend, the reader is referred to the web version of this article.)

8. 根据多年代际石笋记录获得的末次间冰期亚洲季风的准60 年周期

翻译人：杨会会 11849590@mail.sustech.edu.cn

Wang Z J, Chen S T, Wang Y J et al. Sixty-year quasi-period of the Asian monsoon around the Last Interglacial derived from an annually resolved stalagmite δ18O record[J].Paleogeography, Paleoclimatology, Paleoecology, 2020, 541,109545

https://doi.org/10.1016/j.palaeo.2019.109545

摘要：亚洲季风在全新世中后期的 60 年准周期变化在仪器记录和各种陆地记录中广泛存在。然而，这一周期是否存在于更早的间冰期还有待进一步研究。本文以中国永兴洞石笋为研究对象，石笋长 1840 mm，年纹层清晰(生长速率约 1 mm/年)，可重建约 123.20 ~ 121.21 kyr BP 期间的亚洲季风演化序列。石笋记录与 65 ℕ 太阳辐射变化密切相关，表明了太阳辐射对亚洲夏季风的主导控制。从 YX108 记录中移除太阳辐射信号后,剩余的 $\delta^{18}O$ 信号($\Delta\delta^{18}O$)显示 28 个数十年的季风周期。这些波动的平均振幅大于 0.8‰，持续时间一般为 50 ~ 80 年(平均约 64 年)，与全新世中后期亚洲季风变化非常相似。此外，小波分析显示了整个研究时期具有 60 年的显著准周期变化，为评估全新世发现的亚洲季风 60 年准周期性变化是否存在于更老的时期提供了进一步的证据。研究表明，这种准周期变化不仅发生在现代，而且还存在于末次间冰期，其影响甚至可能是亚洲季风系统在冰期-间冰期旋回中的一种内在特征。我们的研究还表明，太阳活动与大西洋多年代际振荡的相互作用可能是亚洲季风 60 年准周期的主要原因。

ABSTRACT: The 60-year quasi-periodic variability of the Asian monsoon in the mid-late Holocene has been found to be widespread in instrumental and various terrestrial records. However, whether this period exists in the older interglacial periods remains to be further studied. This paper is based on an 1840-mm-long stalagmite with clear annual laminae (with a growth rate of about 1 mm/yr) from Yongxing Cave, China, that allows for the reconstruction of the Asian monsoon evolution sequence during the period ~123.20–121.21 kyr BP. The stalagmite record

closely tracks the 65 ℃N solar insolation changes as a whole, indicating the dominant control of solar insolation on the Asian summer monsoon. After removing the solar insolation signal from the YX108 record, the $\delta^{18}O$ residuals ($\Delta\delta^{18}O$) show 28 multidecadal monsoon cycles. The average amplitude of these fluctuations is larger than 0.8‰, with a duration typically ranging from 50 to 80 yr (about 64 yr on average), which is very similar to the mid-late Holocene Asian monsoon variability. Further, wavelet analysis displays a significant quasi-periodicity of 60 years throughout the studied period, providing further evidence for assessing whether the 60-year quasi-periodic variability of the Asian monsoon found in the Holocene exists in older periods. Our study thus suggests that this quasi-periodic variability not only occurred during the modern period but also existed in the Last Interglacial, and their influence may even be an intrinsic characteristic of the Asian monsoon system during glacial-interglacial cycles. We manifested that the interactions between solar activity and the Atlantic Multidecadal Oscillation may be the main reason for the 60-year quasi-period of the Asian monsoon.

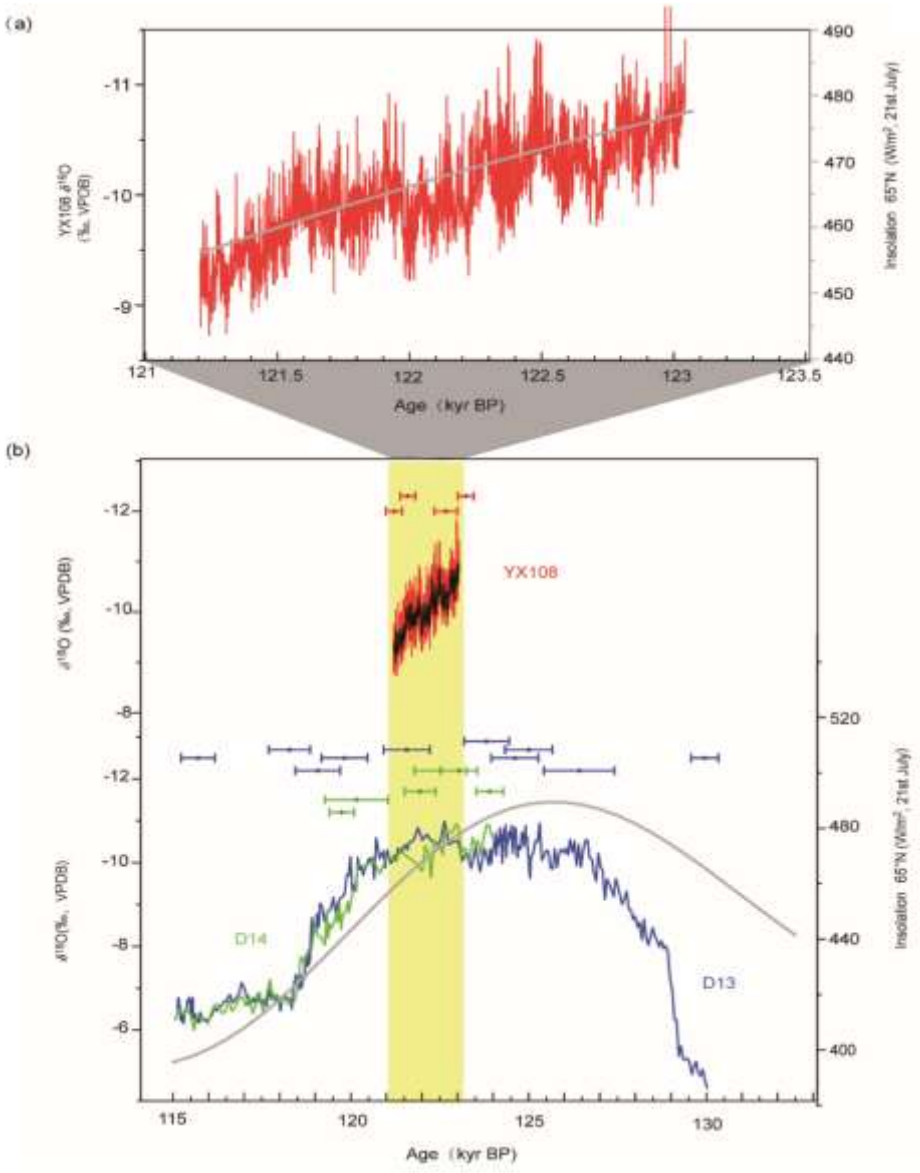

Figure 1. The record of YX108 and its comparison with the Dark Cave stalagmite records in Guizhou during the Last Interglacial. (a) Raw YX108 $\delta^{18}O$ record (red line, this study) and solar insolation curve (gray line) at 65°N on the 21st of July (Berger, 1978). (b) $\delta^{18}O$ time series of stalagmites D13 and D14 from Dark Cave (blue and green lines) (Jiang et al., 2017) and YX108 (red line). The black curve indicates 7-point smoothing, the gray line is the solar insolation curve at 65 ℃N on the 21st of July (Berger, 1978), and the vertical yellow bar denotes the interval from 123.20 kyr BP to 121.21 kyr BP. (For interpretation of the references to colour in this figure legend, the reader is referred to the web version of this article.)

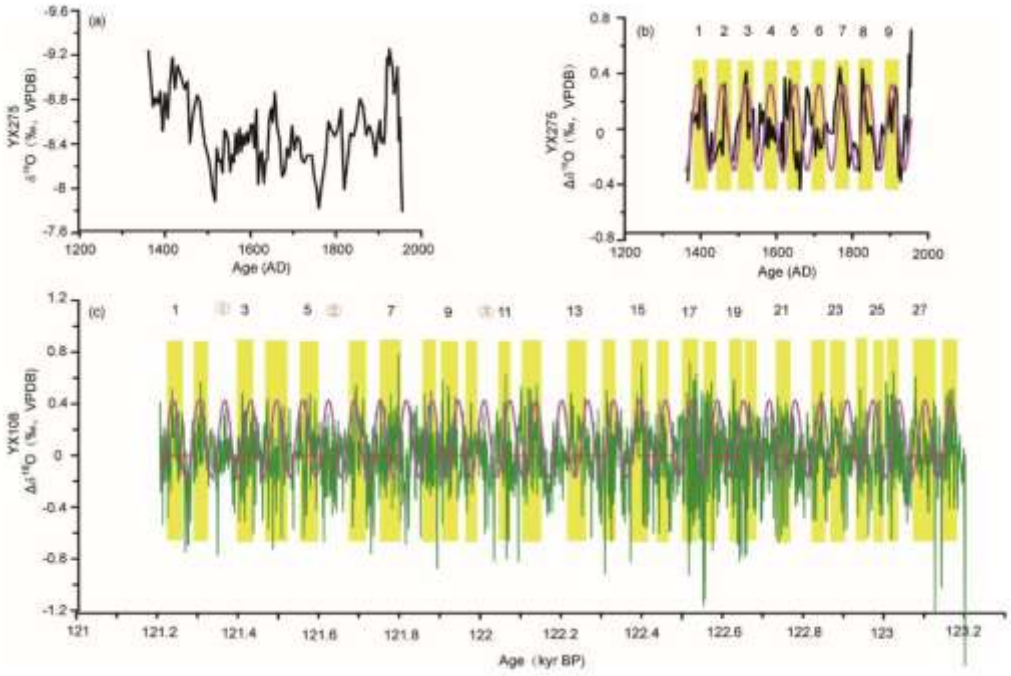

Figure 2. Nearly 60-year cycle characteristics of the interglacial Asian monsoon recorded by stalagmites in Yongxing Cave. (a) YX275 $\delta^{18}O$ (Zhang et al., 2019a). (b)YX275 $\Delta\delta^{18}O$ record (using changepoint, refer to Taylor, 2000). (c) This study. Arabic numbers indicate monsoon climate fluctuations, and the pink lines represent the sine function of 64-year cycles to fit the accuracy of the 60-year quasi-period of fluctuations in both pictures. The horizontal dashed red line depicts mean values of the normalized records. Research indicates that 60-year quasi-period may be an inherent feature of Asian monsoon system during the interglacial periods. (For interpretation of the references to color in this figure legend, the reader is referred to the web version of this article.)

9. 亚北极太平洋与格陵兰岛的风尘记录对比

翻译人：王敦繁 dunfan-w@foxmail.com

Serno, S., G. Winckler, R. F. Anderson, E. Maier, H. Ren, R. Gersonde, and G. H. Haug, Comparing dust flux records from the Subarctic North Pacific and Greenland: Implications for atmospheric transport to Greenland and for the application of dust as a chronostratigraphic tool, Paleoceanography, 2015, 30, 583–600, doi:10.1002/2014PA002748.

摘要：我们以底特律海山钻孔为基础，展示了过去 27000 年以来西亚北极北太平洋(SNP)风尘通量的新记录。将 SNP 尘埃记录与北格林兰冰芯(NGRIP)的风尘记录进行对比，可以发现，在最后一次冰消期，两个地区的风尘变化幅度有显著差异，而突变的时间却是同步的。如果 SNP 中的风尘沉降真实地记录了其在东亚源区的活动，那么其相对振幅的差异一定反映了大气风尘向格陵兰岛输送的气候变化。基于 SNP 和格陵兰岛同步变化的风尘记录，我们把该时期的冰消期突变与 Th^{230} 归一指标和 He^{4} 通量记录对应到相应的过渡的年代来确定 NGRIP 粉尘通量，从而提供了一个新的海洋沉积物的年代地层。该结论得到了放射性碳同位素定年法的佐证，并使我们能够独立地重建放射性碳的古年代。我们发现古化石的年龄在公元前 11.653 年，为 745±140 年即 680±228 年(每小时 14.630 年)。我们重建的古储层年龄与 SNP 西部地区现代地表水储层年龄一致。来自亚南极大西洋和赤道太平洋的风成尘埃记录与来自南极的冰芯记录之间良好的时间同步性，结果支持所提出的尘埃调整方法在全球其他海洋区域更广泛应用的可靠性。

ABSTRACT: We present a new record of eolian dust flux to the western Subarctic North Pacific (SNP) covering the past 27,000 years based on a core from the Detroit Seamount. Comparing the SNP dust record to the North Greenland Ice Core Project (NGRIP) ice core record shows significant differences in the amplitude of dust changes to the two regions during the last deglaciation, while the timing of abrupt changes is synchronous. If dust deposition in the SNP faithfully records its mobilization in East Asian source regions, then the difference in the relative amplitude must reflect climate-related changes in atmospheric dust transport to Greenland. Based

on the synchronicity in the timing of dust changes in the SNP and Greenland, we tie abrupt deglacial transitions in the Th^{230}-normalized He^4 flux record to corresponding transitions in the well-dated NGRIP dust flux record to provide a new chronostratigraphic technique for marine sediments from the SNP. Results from this technique are complemented by radiocarbon dating, which allows us to independently constrain radiocarbon paleoreservoir ages. We find paleoreservoir ages of 745 ± 140 years at 11.653 year B.P., 680 ± 228 years at 14.630 year B.P., and 790 ± 498 years at 23.290 year B.P. Our reconstructed paleoreservoir ages are consistent with modern surface water reservoir ages in the western SNP. Good temporal synchronicity between eolian dust records from the Subantarctic Atlantic and equatorial Pacific and the ice core record from Antarctica supports the reliability of the proposed dust tuning method to be used more widely in other global ocean regions.

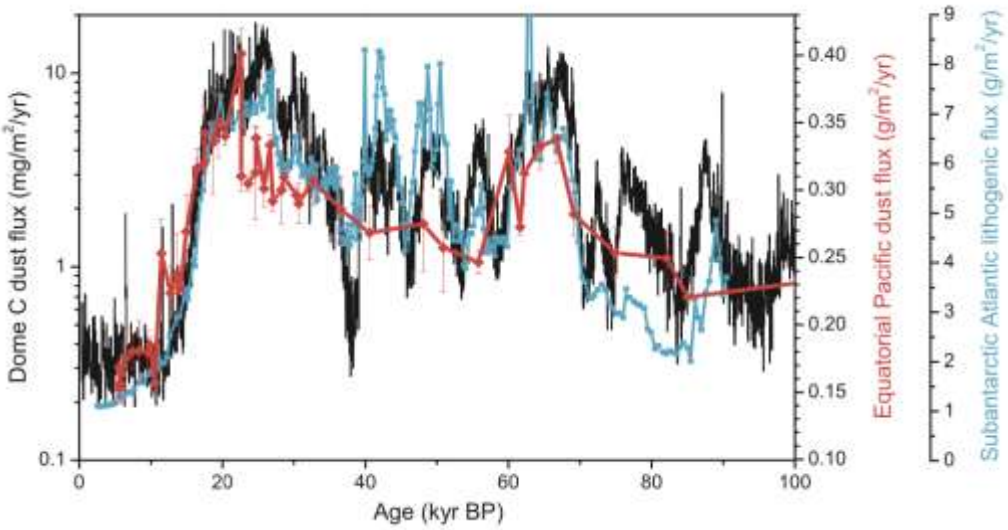

Figure 1. Examples illustrating the potential for global eolian dust records to be used as a chronostratigraphic tool for marine sediment cores. Two marine sediment records of dust flux based on 232Th, one from the equatorial Pacific (red line and diamond symbols; TN013-PC72) [Winckler et al., 2008] and the other from the Subantarctic Atlantic (blue line and square symbols; PS2498-1) [Anderson et al., 2014], showing good temporal synchronicity with the dust flux record from EPICA Dome C in Antarctica (black line) [Lambert et al., 2012] over the last ~100 kyr. Note that the EPICA Dome C ice core record is plotted with a logarithmic scaling.

10. 对于确定环境磁学中磁性矿物组成的特定方法的评估

翻译：王浩森 11849590@mail.sustech.edu.cn

T Qian Y, Roberts A P, Liu Y, et al. 2020. Assessment and Integration of Bulk and Component-Specific Methods for Identifying Mineral Magnetic Assemblages in Environmental Magnetism. 125: e2019JB019024.

Doi: 10.1029/2019JB019024

摘要：在环境研究中，磁学参数被广泛应用于解释磁性矿物组合的变化。传统的室温下对体积磁学参数的测量，例如非磁滞剩磁（ARM）和 ARM 磁化率与磁化率（χ）的比值，可以分别反映沉积物中的磁性矿物浓度和粒径变化，尽管它们不一定非常适合识别磁性矿物组分中的单一磁性成分。一阶反向曲线（FORC）图和低温（LT）测量等更先进的技术可以对磁组分进行更为详细的区分。在这里，我们将常规的体积磁化率的测量与 FORC 图，LT 测量和 X 射线扫描数据，透射电子显微镜以及 FORC 图的主成分分析相结合，以识别和量化地中海东部沉积物中的磁性矿物组合。之所以选择该沉积物是因为它们包含了碎屑，生物成因等磁性矿物组合而成的混合物，这些混合物在不同的有氧（贫有机物）条件下沉积到缺氧（富含有机物）条件下。常规的体积磁学参数可连续记录环境磁学性质的变化，而对选定样品进行的更耗时的 LT 和 FORC 测量可直接对矿物磁组分进行全面地分析，从而能够计算出不同端元对的磁化强度的贡献程度。因此，常规体积磁学参数和先进的磁学技术的结合可以提供环境磁学信号的详细的记录。

ABSTRACT: Magnetic parameters are used extensively to interpret magnetic mineral assemblage variations in environmental studies. Conventional room temperature measurements of bulk magnetic parameters, like the anhysteretic remanent magnetization (ARM) and the ratio of the susceptibility of ARM to magnetic susceptibility (χ), can reflect, respectively, magnetic mineral concentration and/or particle size variations in sediments, although they are not necessarily well suited for identifying magnetic components within individual magnetic mineral assemblages. More advanced techniques, such as first‐order reversal curve (FORC) diagrams and low‐temperature (LT) magnetic measurements, can enable detailed discrimination of magnetic

assemblages. Here, we integrate conventional bulk magnetic measurements alongside FORC diagrams, LT measurements, and X‐ray fluorescence core‐scan data, transmission electron microscope observations, and principal component analysis of FORC diagrams to identify and quantify magnetic mineral assemblages in eastern Mediterranean sediments. The studied sediments were selected because they contain complexly varying mixtures of detrital, biogenic, and diagenetically altered magnetic mineral assemblages that were deposited under varying oxic (organic‐poor marls) to anoxic (organic‐rich sapropels) conditions. Conventional bulk magnetic parameters provide continuous records of environmental magnetic variations, while more time‐consuming LT and FORC measurements on selected samples provide direct ground‐truthing of mineral magnetic assemblages that enables calculation of magnetization contributions of different end members. Thus, a combination of conventional bulk parameters and advanced magnetic techniques can provide detailed records from which the meaning of environmental magnetic signals can be unlocked.

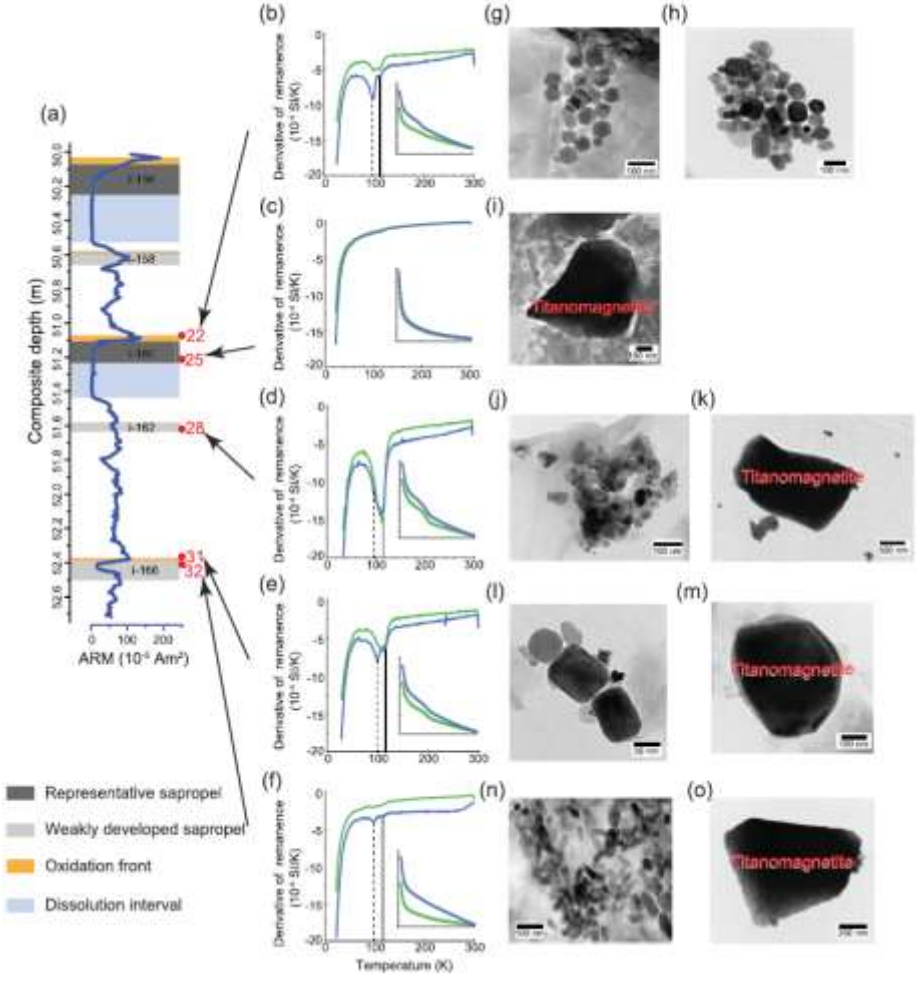

Figure 1. LT magnetic measurements and TEM observations for five representative samples. (a) The locations of the five samples are indicated on an ARM profile with sapropel stratigraphy after Emeis et al. (2000). (b–f) LT magnetization curves (inset) and their derivative curves (larger; ZFC, green; FC, blue). Vertical dashed and solid lines indicate the two distinctive T_v peaks at ~95 and ~110 K, respectively. (g, h) TEM images for Sample 22 from the oxidation front of representative sapropel i‐160 with abundant magnetosomal magnetite; (i) TEM image for Sample 25 from the middle of sapropel i‐160 with a detrital titanomagnetite particle; (j, k) TEM images for Sample 28 from the middle of weakly developed sapropel i‐162 with both magnetosomal magnetite and titanomagnetite; (l, m) TEM images for Sample 31 from the oxidation front above weakly developed sapropel i‐166 with clusters of biogenic magnetite and detrital titanomagnetite; and (n, o) TEM images for Sample 32 from the middle of weakly developed sapropel i‐166 with abundant bullet‐shaped biogenic magnetite and detrital titanomagnetite. TEM electron dispersive X‐ray (TEM‐EDX) spectra are indicative of mineralogy, as shown in Figure S2.

11. 沉积赤铁矿(α-Fe_2O_3)磁学方法的定量：现有方法的限制与发展方向

翻译人：张伟杰 1312390861@qq.com

Roberts AP, Zhao X, Heslop D, et al. Hematite (α-Fe2O3) **quantification in sedimentary magnetism: limitations of existing proxies and ways forward**. Geoscience Letters. 2020, 7(1). *https://doi.org/10.1186/s40562-020-00157-5*

摘要：测定赤铁矿对沉积磁化作用的贡献是定量环境研究中的一项重要而困难的任务。赤铁矿纳米颗粒的结晶差和粒度细特性使得矿物学和光谱方法对自然环境中赤铁矿的浓度进行量化具有挑战性，然而赤铁矿较弱的磁化强度以及纳米颗粒聚集体具有超顺磁特征使得利用剩磁测量将赤铁矿定量化变的困难。S-ratio 与 HIRM 等常用的磁学参数倾向于低估相对赤铁矿含量和绝对赤铁矿含量。虽然分解等温剩磁获得曲线（IRM）确定磁性矿物贡献的方法具有被低估的不确定性，但是这种方法是将赤铁矿定量较适当的方法之一。漫反射光谱等方法可以在一定条件下定量测定赤铁矿和针铁矿的相对含量。综合使用磁学、矿物学和光谱方法对估算的赤铁矿含量提供了有价值的互相检验，推荐使用综合的方法进行相关研究。今后还需要进一步的工作来提升和发展的赤铁矿定量的方法。

ABSTRACT: Determination of hematite contributions to sedimentary magnetizations is an important but difficult task in quantitative environmental studies. The poorly crystalline and fine-grained nature of hematite nanoparticles makes quantification of their concentrations in natural environments challenging using mineralogical and spectroscopic methods, while the weak magnetization of hematite and often significant superparamagnetic nanoparticle concentrations make quantification difficult using magnetic remanence measurements. We demonstrate here that much-used magnetic parameters, such as the S-ratio and ‘hard’ isothermal remanent magnetization (HIRM), tend to significantly underestimate relative and absolute hematite contents, respectively. Unmixing of isothermal remanent magnetization (IRM) acquisition curves is among the more suitable approaches for defining magnetic mineral contributions, although it has under-appreciated uncertainties that limit hematite quantification. Diffuse reflectance spectroscopy and other

methods can enable relative hematite and goethite content quantification under some conditions. Combined use of magnetic, mineralogical, and spectroscopic approaches provides valuable cross-checks on estimated hematite contents; such an integrated approach is recommended here. Further work is also needed to rise to the challenge of developing improved methods for hematite quantification.

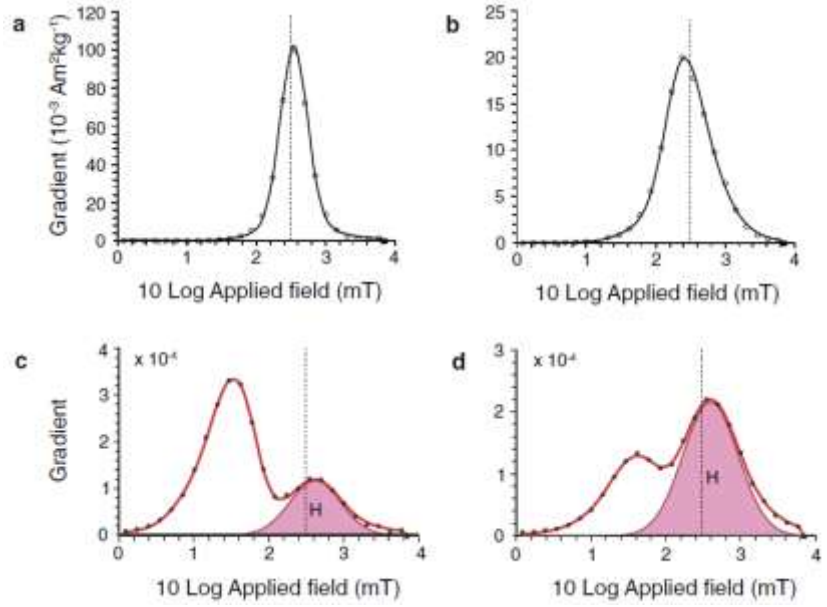

Figure 1. First derivative of IRM acquisition (gradient) curves and hematite components for 7-T maximum applied fields. Results for hematite pigments in a decorative ‘print stone’ from the Mount McRae Shale Formation, Western Australia (Abrajevitch et al. 2014): a hematite print stone pigment (sample pps11) and b uniform pigment (sample TOM07). Results from Abrajevitch et al. (2015) for: c Paleogene limestone 21 cm above the K–Pg boundary at Bottaccione Gorge, Italy, and d limestone 46.5 cm below the boundary. Abrajevitch et al. (2015) identified five components; for clarity, only the hematite (labelled H) component of interest here is shown. Dashed vertical lines represent the 300-mT cut-off field.

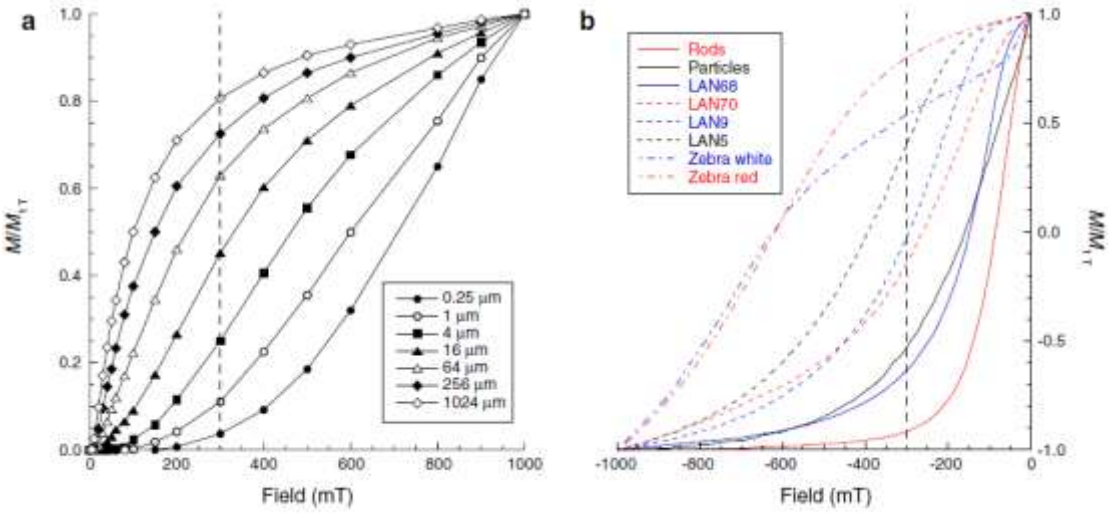

Figure 1. IRM acquisition and backfield demagnetization curves for hematite samples. a IRM acquisition curves for known hematite size fractions, where finer sizes are more resistant to acquisition (and vice versa). Redrawn from Thompson (1986). b Backfield demagnetization curves for SD hematite samples measured at the Australian National University (where DC demagnetization curves are equivalent to IRM acquisition curves with twice the amplitude and opposite slope for non-interacting SD particles). Two samples (particles, zebra white) have steep initial slopes due to magnetically soft hematite near the superparamagnetic/SD threshold size and are then dominated by higher coercivities. Zebra samples are pigmentary hematite from Abrajevitch et al. (2018). LAN samples are natural nanocrystalline hematite samples from deeply weathered regolith from Lancefield South gold mine, Western Australia. 'Particles' are equidimensional hematite nanoparticles (45–85 nm particle sizes) and 'rods' are nanorods (250–350 nm (length) × 50–100 nm (width)) that were synthesized hydrothermally (Islam et al. 2012). Dashed vertical lines represent the 300-mT cut-off field.

12. U1480E 与 U1489H 孔沉积物磁化率各向异性特征：自然沉积或人工成因对古地磁的影响

翻译人：李海 12031330@mail.sustech.edu.cn

Yang T , Zhao X , Petronotis K , et al. ***Anisotropy of Magnetic Susceptibility (AMS) of Sediments From Holes U1480E and U1480H, IODP Expedition 362: Sedimentary or Artificial Origin and Implications for Paleomagnetic Studies[J].*** Geochemistry, Geophysics, Geosystems, 2019, 20(11).

摘要：识别取样过程引起的扰动不是一件容易的事，这对于弱磁化沉积物的古地磁研究是必不可少的。本文，我们报告了苏门答腊俯冲带以西 IODP 362 航次 U1480E 和 U1480H 孔的沉积物的磁化率（AMS）各向异性和古地磁数据。 AMS 的特征是未受干扰的沉积物中陡峭的最小主轴（Kmin）。然而，相当一部分回收的沉积物受到明显的取芯诱发的扰动的影响。在这些情况下，我们观察到了三种 AMS 模式：（1）AMS 主轴随机分布于具有混合和变形床层的沉积物中；（2）具有向上拱形床的沉积物的 Kmin 轴偏离工作面的分裂面一半；（3）吸入沉积物的特征是垂直的 Kmax 轴。这些与变形有关的 AMS 模式可归因于取芯过程和后续采样程序引起的矿物颗粒的重新排列。除了低矫顽力、垂直、钻孔引起的叠印外，我们还观察到了高矫顽力成分，它可能是初级磁化强度与钻孔叠印的抗退磁部分的组合。在考虑了扰动间隔之后，可以在未扰动的沉积物中识别出几个极性转变，这些转变与更新世地磁极性时标有很好的相关性。这些观察结果表明，将地质意义归因于从软沉积岩心获得的 AMS 和古地磁数据时要格外谨慎，因为软沉积岩心很容易受到岩心诱发的干扰。此外，AMS 测量提供了一种潜在的工具，可用于识别岩心变形以进行进一步的古地磁研究。

Abstract Recognition of coring-induced disturbance, which is essential for magnetic fabric and paleomagnetic studies of poorly lithified sediments, is generally not straightforward. Here, we report on anisotropy of magnetic susceptibility (AMS) and paleomagnetic data of the sediments from Holes U1480E and U1480H, IODP Expedition 362, west of the Sumatra subduction zone.

AMS is characterized by steep minimum principal axes (Kmin) in undisturbed sediments. However, a considerable portion of the recovered sediments are affected by significant coring-induced disturbance. In these cases, we observed three AMS patterns: (1) AMS principal axes are randomly distributed for sediments with mingling and distortion of beds, (2) Kmin axes of sediments with upward‐arching beds are deflected out of the splitting face of the working half, and (3) suck-in sediments are characterized by vertical Kmax axes. These deformation‐dependent AMS patterns can be attributed to the realignment of mineral particles caused by the coring process and subsequent sampling procedures. Besides a low-coercivity, vertical, drilling-induced overprint, we observed a high‐coercivity component that is likely a composite of the primary magnetization with a demagnetization‐resistant portion of the drilling overprint. After accounting for the disturbed intervals, several polarity transitions can be identified in the undisturbed sediments which correlate well with the Pleistocene geomagnetic polarity timescale. These observations demonstrate that great caution is required when attributing geological significance to AMS and paleomagnetic data obtained from soft sediment cores, which are highly susceptible to coring‐induced disturbance. In addition, AMS measurements provide a potential tool for identifying core deformation for further paleomagnetic studies.

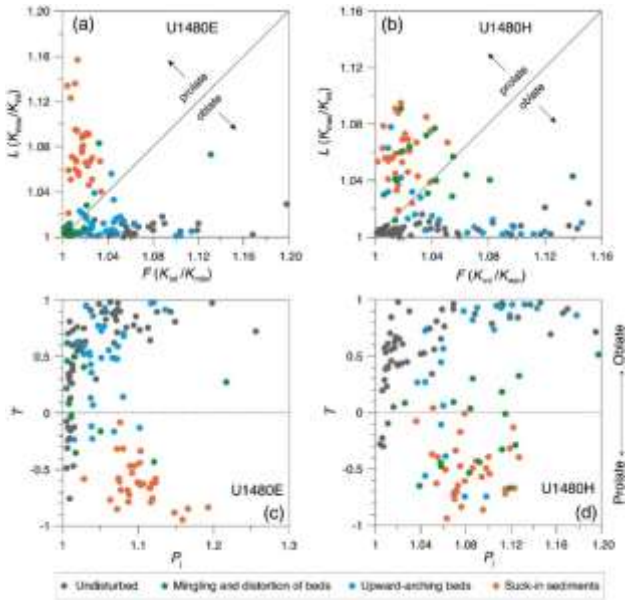

Figure 1. Lineation L is plotted versus foliation F in a Flinn‐type diagram for Holes (a) U1480E and (b) U1480H. (c, d) Relationship between the corrected anisotropy degree Pj and the shape parameter T.

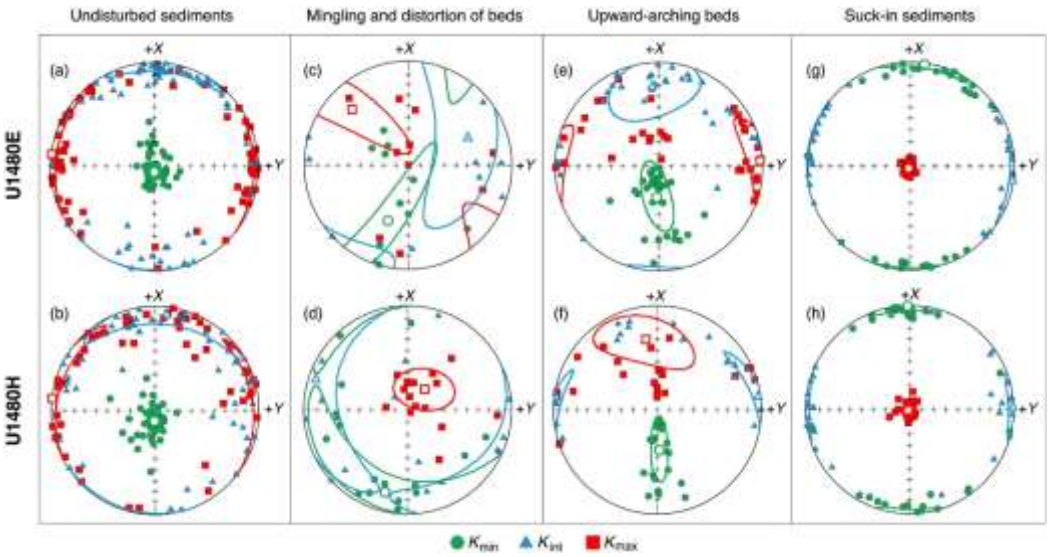

Figure 2. Lower hemisphere, equal‐area projections that show the directions of the three principal AMS axes in core coordinates of sediments with different coring disturbances from Holes U1480E and U1480H. Large open symbols show the mean directions of the three principal susceptibility axes calculated with Jelínek's statistics (Jelínek, 1981). Ovals surrounding mean directions are 95% confidence ellipses.